Shared Transcriptomic Signatures Reveal Synaptic Pruning as a Link Between Alzheimer's Disease and Epilepsy

Huihong Li[1,2,3,4], Zhiran Xie[4], Yuxuan Tian[4], Bingying Lin[1,2,3,5], Jianwei Li[1,2,3,5], Jie Wu[1,2,3], Mingjie Chen[6], Xueke Liu[6], Yushan Sun[6], Si Chen[1,2,3,5], Zihan Deng[1,2,3,5], Mengqi Hong[1,2,3,5], Bing Huang[1,2,3,5], Naili Wei[1], Xiaoyu Ji[1,2,3,5*]

[1]Department of Neurosurgery, The First Affiliated Hospital of Shantou University Medical College, Shantou, Guangdong 515041, China

[2]Brain Function and Disease Laboratory, Shantou University Medical College, Shantou, Guangdong 515041, China

[3]Department of Pharmacology, Shantou University Medical College, Shantou, Guangdong, 51504, China

[4]Program in Computational Biology and Biomedical Informatics, Yale University, New Haven, Connecticut, United States of America

[5]Pain and Related Diseases Research Laboratory, Shantou University Medical College, Shantou, Guangdong 515041, China

[6]Department of Biotechnology and Food Engineering, Guangdong Technion – Israel Institute of Technology, Shantou, China 515063

[*]**Corresponding authors**
Contact: Dr. Xiaoyu Ji, xyji@stu.edu.cn;

Keywords: Alzheimer's disease, epilepsy, synaptic pruning, computational neuroscience, modeling, transcriptome, *Tyrobp*, *Trem2*, *C1q*

Highlights

Transcriptomic analysis across epilepsy (EP) and Alzheimer's disease (AD) models and patient datasets revealed a conserved immune gene module.

Tyrobp-Trem2-C1q microglial synaptic pruning pathway was identified as a central shared molecular mechanism across datasets.

Computational modeling revealed that preferential pruning of inhibitory synapses alters E/I balance toward excitability and increases synchrony in neural network

Graphic abstract

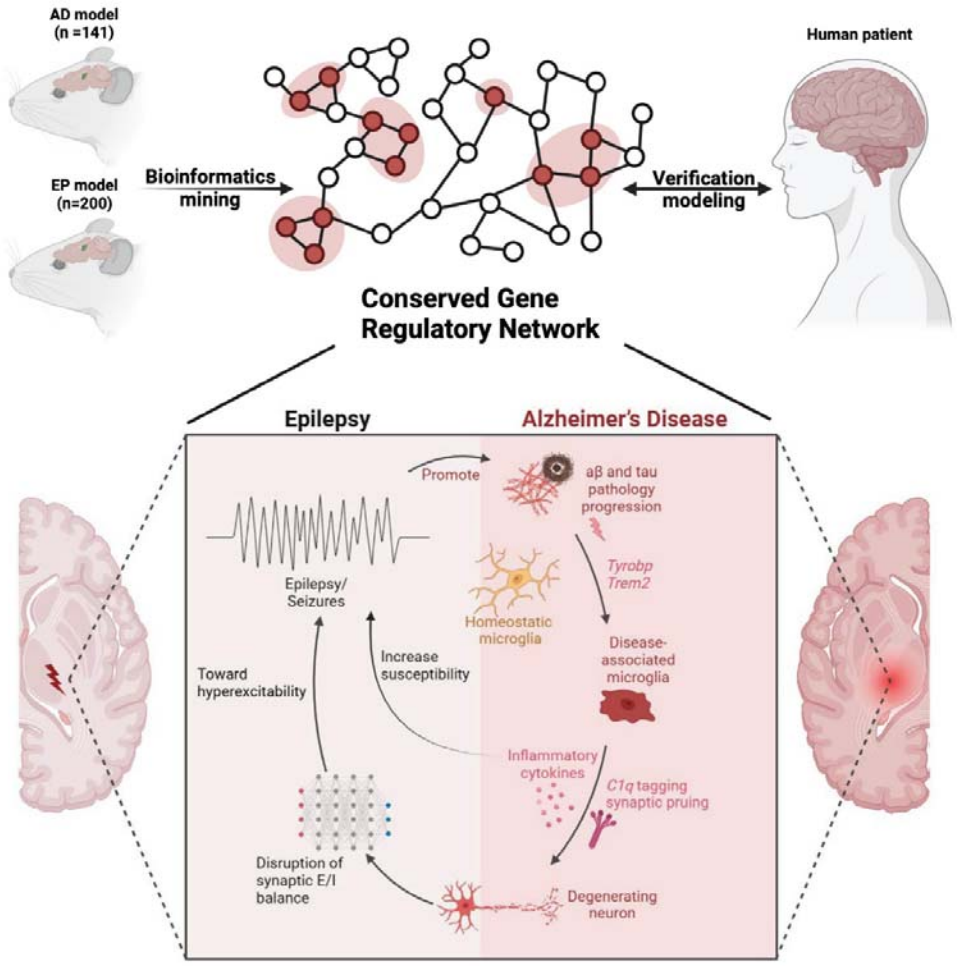

Abstract

Alzheimer's disease (AD) and epilepsy (EP) share a complex, bidirectional relationship, yet the molecular basis of their comorbidity remains elusive. To address this, we analyzed publicly available large-scale transcriptomic datasets from pilocarpine-induced EP mouse models (n=200), two AD mouse models expressing human tau (rTg4510, TG) or amyloid precursor protein (J20) (n=141), and transcriptomic profiles from AD and EP patient cohorts. Differential expression and weighted gene co-expression network analyses revealed a highly conserved immune-related module enriched in microglia-specific genes, centered around *Tyrobp*, *Trem2*, and *C1q* complement component genes (*C1qa*, *C1qb*, *C1qc*) involved in the synaptic pruning pathway. Gene regulatory network analysis showed that *Tyrobp* regulates these *C1q* components gene through *Trem2*. These hub genes were markedly upregulated in both models and human patient datasets, preserved their regulatory relationship across species, and displayed strong diagnostic value. Cell composition deconvolution and single-cell transcriptomics confirmed their high, cell-type-specific expression in microglia from both animal model and human patient datasets. Moreover, computational modeling indicated that excessive synaptic pruning, particularly of inhibitory synapses, alters the excitation/inhibition (E/I) balance toward excitability that increases neural network synchrony. Collectively, our findings reveal how microglial complement-driven synapse elimination may promote both seizure activity and cognitive decline. We suggest that microglia play a central role in the comorbidity of EP and AD, and further exploration of this synaptic pruning pathway in the context of EP may provide promising insights into the treatment of AD and EP comorbidity.

1. Introduction

Alzheimer's disease (AD) and epilepsy (EP) are two common neurological diseases with a complex bidirectional relationship that contributes to their respective pathogenesis [1–3]. AD, characterized by progressive cognitive decline and neurodegeneration, is the leading cause of dementia worldwide and affects an estimated 55 million people worldwide. This number is expected to triple by 2050 as life expectancy increases [4]. EP, characterized by recurrent unprovoked seizures, affects more than 50 million people worldwide with a particularly high incidence among elderly populations, especially those with neurodegenerative conditions such as AD [5,6].

Epidemiological studies have revealed a complex interplay between AD and EP. AD patients show increased susceptibility to EP, with 10–22% experiencing unprovoked seizures, while 22–54% demonstrating subclinical epileptiform activity during disease progression [7,8]. These seizures, predominantly occurring in the temporal lobe, correlate with accelerated cognitive decline and enhanced AD pathology [9]. Conversely, EP patients exhibit a two-fold higher risk of developing dementia compared to controls, with late-onset EP patients showing a three-fold increased risk [10,11]. This elevated risk is particularly evident in temporal lobe epilepsy (TLE), where numerous pathological features overlap with AD [9].

Both diseases show overlapping pathological characteristics, especially in TLE, including amyloid deposition, tau pathology, and hippocampal sclerosis [12,13]. Chronic seizures increase neuronal activity and metabolic demands, potentially accelerating the production and aggregation of amyloid-β (aβ) and hyperphosphorylated tau protein [14,15]. Conversely, the progressive accumulation of these pathological proteins in AD may lower seizure thresholds, promoting hyperexcitability and epileptiform activity [16,17]. Furthermore, neuroinflammation, synaptic loss, and microglial activation, features of both AD and TLE, may synergistically accelerate neuronal damage and network dysfunction [18,19], potentially explaining the high comorbidity rates observed clinically.

The molecular mechanisms underlying this comorbidity remain incompletely understood, though mounting evidence suggests shared molecular pathways driving neuronal hyperexcitability and protein aggregation in both disorders [20]. Recent findings implicate dysregulated protein homeostasis, mitochondrial dysfunction, and chronic inflammatory responses as central contributors [7,19,21]. Additionally, alterations in glutamatergic and GABAergic signaling, alongside disruptions in synaptic plasticity pathways, appear to converge in both conditions, particularly within the hippocampal region [22–24].

The treatment of EP in AD patients has been considered a complex clinical challenge in terms of the decision to treat seizures and the choice of antiseizure medications [25]. Emerging therapeutic approaches, including targeted immunotherapies and novel small molecules, show promise but require a deeper understanding of the shared pathological mechanisms. Therefore, systems biology and computational modeling approaches are urgently needed to integrate insights from animal models and patients. Such approaches could reveal common molecular pathways, cellular processes, and neural network dynamics alterations underlying this comorbidity, which is crucial for developing more effective, targeted therapeutic strategies.

To address this gap, we hypothesize that conserved molecular pathways exist in AD and EP animal models and human patients. To test this, we (1) analyzed and integrated large-scale transcriptomic data from pilocarpine-induced EP mouse models (n=200), two AD mouse models expressing human tau (rTg4510, TG) or amyloid precursor protein (J20) (n=141) to identify shared transcriptional signatures and pathways; (2) validated these findings in AD and EP human patient datasets; and (3) developed computational models to link molecular insights to network mechanisms of epileptogenesis. Our analysis identified a conserved synaptic pruning pathway involving *Tyrobp*, *Trem2*, and *C1q* complement genes. Computational modeling further suggested that preferential synaptic elimination of inhibitory synapses contributes to neuronal network excitability and the cognitive decline associated with this comorbidity.

2. Materials and Methods

2.1 Data Collection

A comprehensive database search was conducted to retrieve transcriptomic data from AD and EP models as well as human patients. Databases including Gene Expression Omnibus (GEO) and European Nucleotide Archive (ENA), were searched using the keywords “epilepsy” and “Alzheimer's disease”. We downloaded and reanalyzed two extensive bulk RNA-seq datasets from EP and AD mouse models. The EP model dataset was obtained from the ENA (PRJEB18790), and includes bulk RNA-seq data from 200 hippocampi of pilocarpine-induced EP model mice and wild-type (WT) control. The AD dataset was downloaded from GEO (GSE125957), and includes bulk RNA-seq data from 141 samples of the entorhinal cortex and hippocampus of AD model mice that expressed either human tau (rTg4510, TG) or amyloid precursor protein (J20), with their corresponding healthy controls at various ages (range from 2 to 12 months).

To assess the clinical relevance of insights derived from animal models at the gene, pathway, and cellular levels, we also retrieved and analyzed several large-scale transcriptome datasets from AD and EP patients. For cross-species validation of

disease co-expression modules, we used 129 hippocampal samples from TLE patients (GSE63808) and 97 middle temporal gyrus samples from AD patients (GSE132903). To evaluate the diagnostic value of shared transcriptional signatures, we analyzed 47 hippocampal samples from EP patients and controls (E-MTAB-3123), along with 253 different brain region samples from AD patients and controls (GSE48350). Finally, single-cell RNA sequencing (scRNA-Seq) data from 85,780 immune cells of six drug-refractory EP patients (GSE201048) and single-nucleus RNA sequencing (snRNA-Seq) data from 174,420 immune cells from 217 AD patients and 226 controls (GSE227223) were employed to identify the cell types and subtypes expressing these shared transcriptional signatures.

2.2 Quality control and preprocessing

All the downloaded raw RNA sequences of AD and EP model datasets were processed for quality check and trimmed to acquire clean sequences using FastQC (0.12.1) and Fastp (0.22.0) with stringent parameters (--qualified_quality_phred 30 --n_base_limit 5 --detect_adapter_for_pe --cut_tail --trim_front1 15 --dedup --trim_poly_x --trim_poly_g) to ensure high data quality [26,27]. Ribodetector (0.2.7) was used to remove potential rRNA contamination [28]. Low-quality regions in the sequences, attributed to instability in the sequencing platform, were also trimmed using Fastp. Trimmed sequences were then aligned to the GRCm39.111 reference mouse genome using HISAT2 (2.2.1) [29] and followed by quantification using featureCounts (2.0.6) [30].

For the AD model dataset, samples were excluded from subsequent analysis based on the criteria outlined in the original publication, resulting in 121 high-quality RNA-seq samples. For the EP model dataset, duplicate and low-quality samples were initially removed. Then a variance-stabilizing transformation was applied to the count matrix before performing Principal Component Analysis (PCA) to identify potential outlier samples. PCA was then performed to identify outliers, with Mahalanobis distances calculated from PCA scores. A chi-squared distribution threshold of 0.975 was used to detect significant outliers, resulting in 11 samples subsequently excluded from analysis. Detailed information on quality control and mapping metrics is provided in **Table S1**. Following quality control, mapping, and exclusion of low-quality samples, no significant differences in read depth were observed between model groups and controls.

2.3 Differential Expression Analysis

Differential expression analysis was conducted using DESeq2 (1.46.0) [31]. Before analysis, non-expressed and lowly expressed genes were filtered out. For the EP model dataset, only genes with at least 20 counts in a minimum of 90 samples (~90 samples per group) were retained, while for the AD dataset, genes with at least 20 counts in at least 6 samples (6–8 samples per group) were kept. The DESeq function was then used to estimate size factors and dispersions and to perform statistical testing

for differential expression [31].

For the EP model dataset, the design formula was specified as ~Condition (EP/WT), and results were extracted by comparing the "EP" condition to the "WT" condition. For the AD dataset, we aimed to detect progressive differentially expressed genes (DEGs), following a previous approach [32], using DESeq's likelihood-ratio test to fit the statistical model: *Gene expression* = *Genotype* + *Age* + *Genotype* × *Age* (Interaction). P-values were adjusted for multiple testing using the Benjamini-Hochberg (BH) correction.

DEGs were identified based on an adjusted p-value < 0.05 and |log2 fold change| > 1. These thresholds were applied to the EP model dataset and to the final time point of the AD dataset. Shared DEGs between the EP and AD model datasets were identified by taking the intersection of their DEG results. Kyoto Encyclopedia of Genes and Genomes (KEGG) pathway and gene ontology (GO) analyses for shared DEGs were performed using WebGestalt (2024), with weighted set cover redundancy removal [33].

2.4 Weighted Gene Co-expression Network Construction

To construct weighted gene co-expression networks and compare results from EP and AD model datasets, we employed a standard meta-WGCNA comparison method [34–36]. All datasets underwent variance-stabilizing transformation using DESeq2 (1.46.0) to normalize the variance across different samples. We then calculated the median absolute deviation (MAD) and retained the top 85% of genes with the highest MAD in each dataset, resulting in 10,997 genes common to all datasets for comparability in further analyses. Outliers were identified through hierarchical clustering, excluding two samples from the rTg4510 dataset and three from the J20 dataset. To assess dataset comparability, general network properties such as average gene expression and overall network connectivity were calculated.

We constructed signed co-expression networks using the WGCNA R package (1.73) [35], selecting the lowest soft-thresholding power to achieve a scale-free topology fit index (R^2) of at least 0.85 across datasets. Adjacency matrices were generated using the signed network option and converted to topological overlap matrices (TOM) to quantify similarity in gene connectivity profiles. Modules were identified by average linkage hierarchical clustering of TOM dissimilarity (1-TOM), followed by dynamic tree cutting with parameters deepSplit = 2 and minClusterSize = 24. This procedure was also applied to patient microarray datasets (GSE63808 and GSE132903), using variance-stabilizing normalization with the “limma” (3.62.1) package [37].

To match modules between EP and AD model datasets, we color-mapped the AD modules to the best matching EP modules according to the hypergeometric test [34]. Module profiles were summarized using module eigengenes (MEs), derived from the

first principal component of each module. To identify modules significantly associated with disease genotypes (EP or interaction of TG/J20), we calculated Pearson correlation coefficients between MEs and genotype information, with significance defined as $p < 0.05$ and an absolute correlation coefficient > 0.65 [38]. Module membership (MM) and gene-genotype significance (GS) were also determined by calculating Pearson correlations between individual genes and MEs or genotypes, respectively. KEGG pathway and GO analyses for module annotation were conducted using WebGestalt (2024) with weighted set cover redundancy removal [33].

2.5 Module Preservation Analysis

To assess module preservation of the EP model module in AD model datasets, we used two approaches [40]: Zsummary preservation statistics and cross-tabulation-based preservation statistics.

We employed the modulePreservation function from the WGCNA R package, with parameters set to networkType="signed", nPermutations=100, to calculate composite Z-summary preservation statistics. This metric evaluates preservation based on module size, network density, and connectivity, offering a comprehensive assessment of how well the structure of EP modules is maintained in AD datasets. The Z-summary thresholds were interpreted as follows: Z-summary > 10 indicates strong evidence of preservation, 2 < Z-summary < 10 suggests moderate evidence, and Z-summary < 2 indicates no evidence of preservation [40]. To complement the Z-summary statistic, we also used the medianRank preservation statistic, which assesses relative preservation across modules with less dependency on module size. A lower median rank denotes stronger observed preservation [49].

Additionally, we used a cross-tabulation method to examine module overlap between EP and AD model datasets, as well as between model and patient datasets (GSE63808 and GSE132903). This method generates a contingency table reporting the overlapping gene number between each module in the reference and test datasets [49]. The statistical significance of overlaps was assessed using Fisher's exact test, with p-values adjusted using the BH correction. A module was reported as significantly overlapping if the overlap count was > 30 and the adjusted p-value was < 0.05.

2.6 Hub Gene Identification and Regulatory Network Analysis

Hub genes act as key drivers within a module and were identified using stringent criteria to minimize false positives: genes ranking in the top 10% for intramodular connectivity within each module, MM > 0.9, and GS > 0.4. Shared hub genes were determined by intersecting the hub genes of key modules in both EP and AD datasets, along with the DEGs. The expression and diagnostic value of these shared hub genes were further explored in the AD and EP patient datasets (GSE48350 and E-MTAB-3123).

To further explore interactions and potential regulatory relationships among shared hub genes in the EP and AD model datasets, we constructed a protein-protein interaction (PPI) network using the STRING database (12.0) (https://string-db.org/cgi/input.pl) with a confidence score threshold of 0.4 and a false discovery rate (FDR) of 5% [41]. We then performed regulatory network analysis with the GENIE3 (1.28.0) algorithm, which applies a random forest approach to infer potential regulatory relationships from gene expression data. GENIE3 ranks regulatory interactions by weight, with higher weights indicating stronger regulatory links [42]. Gene expression profiles of the key module from the EP and TG model datasets were used to infer plausible regulatory interactions among shared hub genes. To reduce false positives, a weight threshold of 0.01 was applied to filter out weaker regulatory links. Additionally, only the top 30 plausible regulatory links between shared hub genes were retained to construct gene regulatory networks. Finally, the shared regulatory network of hub genes was constructed by intersecting the regulatory networks inferred from the EP and TG model datasets.

2.7 Machine Learning

To validate the diagnostic value of the transcriptomic signatures identified in animal models, multiple machine-learning models were used to train diagnostic models based on these signatures in EP and AD patient datasets (GSE48350 and E-MTAB-3123) to predict disease status based on gene expression profiles. The main goal was to distinguish patients with AD or EP from healthy controls. First, the gene expression data was standardized by applying the StandardScaler function in the sklearn.preprocessing module in Python. Standardization ensures that all features/gene signatures have a mean of 0 and a standard deviation of 1, making them comparable across scales. Several machine learning algorithms were used in the classification process, including logistic regression, support vector machine (SVM), random forest, naive Bayes, XGBoost, AdaBoost, and CatBoost. To evaluate the performance of each model, a 5-fold stratified cross-validation (CV) method was used. Different metrics were used to measure the performance of the models, including accuracy, precision, recall, F1 score, and AUC. The ROC curve and AUC score for each classifier were plotted to visually examine the trade-off between sensitivity and specificity.

2.8 Cell Composition Deconvolution

In silico deconvolution can estimate the cellular composition of a tissue sample from its gene expression profile, with CIBERSORT particularly suited for cellular composition deconvolution of brain transcriptomes [43,44]. The raw count expression matrix was converted to FPKM values using edgeR (4.4.1) [45], followed by cell composition deconvolution using CIBERSORT (1.04**)** via the BrainDeconvShiny platform, with cell-type signatures specific to *Mus musculus* from immunopurified

mouse brain tissue [44,46]. For statistical analysis, the Mann-Whitney test ($p < 0.05$) was applied to compare the EP dataset with the control group, while the Kruskal-Wallis test was used for the AD datasets, followed by pairwise comparisons across age and genotype groups. The BH method was used to control the FDR ($q < 0.05$). Associations between identified cell types and shared hub genes were determined by calculating Pearson correlation coefficients.

2.9 Single-cell and Single-nucleus RNA Sequencing Data Analysis

To localize and validate the expression of transcriptomic signatures identified in animal models at the cellular level in AD and EP patients, count matrices of sc/snRNA-seq (GSE201048 and GSE227223) were downloaded and processed according to the methods outlined in the original publications [47–49]. Quality control was performed by filtering cells with high mitochondrial content (>20% for the EP dataset and >5% for the AD dataset) and selecting cells based on cellular complexity (300–5,000 genes per cell for the EP dataset and >500 genes for the AD dataset). Subsequent data processing was conducted using the standard Seurat pipeline, including scaling, normalization, variable gene identification, and clustering. PCA was performed on the 2,000 most variable genes, with the first 20 principal components (PCs) used for t-SNE and clustering in the EP dataset, and the first 30 PCs used for the AD dataset. Cluster identities were determined by identifying DEGs with the FindMarkers function, followed by annotation based on the original publications. For the AD dataset, only single nuclei from AD patients were used for visualizing expression distributions of shared hub genes across clusters.

2.10 Computational modelling

To explore the contribution of the identified key pathways to pathological changes in AD and EP at the network level, we implemented a spiking neural network using the Izhikevich neuron model to simulate hippocampal CA3 circuit dynamics with simulation spans of 1000ms, employing the Brian2 package [50]. The network consists of 1000 neurons (800 excitatory and 200 inhibitory), with dynamics governed by the Izhikevich equations [51]:

$$\frac{dv}{dt} = 0.04v^2 + 5v + 140 - u + I$$

$$\frac{du}{dt} = a(bv - u)$$

where v is the membrane potential, u is the recovery variable. When $v \geq 30$ mV, the following reset conditions are applied: $v = c;\ u = u + d$. Parameters a, b, c and d are set to standard regular spiking for excitatory neurons and fast-spiking for inhibitory neurons following the Izhikevich framework [51]. I is external input incorporating both suprathreshold Poisson noise at 1 Hz and presynaptic inputs [51].

Following Liu's EP network modeling, synaptic connectivity is sparse, with a 0.1

probability of random connections between neurons, and interactions are modeled using conductance-based synapses to allow for voltage-dependent temporal and spatial summation [51]. Synaptic interactions simulate AMPA (excitatory) and GABA-a (inhibitory) currents for four connection types: excitatory-excitatory (E→E), excitatory-inhibitory (E→I), inhibitory-excitatory (I→E), and inhibitory-inhibitory (I→I) [51]. Synaptic currents are calculated as [52]:

$$I_j = wS_{i\to j}(t)\left(E_i - v_j\right)$$

we introduce w to leverage the synaptic weight, while $S_{i\to j}(t))$ is the synaptic conductance evolving as $\frac{dS_{i\to j}(t)}{dt} = -\frac{S_{i\to j}(t)}{\tau(i)}$ and E_i is the synaptic reversal potential [51]. Synaptic conductance is updated upon presynaptic spikes by adding a peak conductance $S_{i\to j}(max)$, while we calibrate unitary synapse to induce EPSPs for E→E/E→I and IPSPs for I→E/I→I of 1.0, 2.5, −2.0, −1.0 mV with time constants:$\tau = \{3, 3, 5, 5\}$ ms and reversal potentials:$E = \{0, 0, -75, -75\}$ mV [53–55]. Each of four types of synaptic weights (w) are drawn independently from a standard normal distribution, normalized to [0, 1], and set to 0 during synaptic pruning. We simulated synaptic pruning by selectively removing excitatory (E→E and E→I) or inhibitory (I→E and I→I) synapses, starting with those having the lowest weights based on the synaptic weight distribution (ranging from 0% to 50%, with 5% increments). This approach was designed to mimic the excessive pruning of excitatory synapses observed in AD or the loss of inhibitory synapses seen in EP. Each pruning simulation was repeated at least 50 times.

The excitation/inhibition (E/I) ratio quantifies the balance between synaptic drives in the network, indicating firing rate stability, while event synchrony measures temporal coordination of firing patterns, implying network oscillation patterns. Both large E/I ratio and excessive synchrony are associated with EP and AD [52].

To analyze the network, we calculated the E/I ratio and event synchrony to measure the effects of synaptic pruning on firing rate stability and temporal coordination. The E/I ratio compares total excitatory currents (from E→E and E→I synapses) to the absolute magnitude of inhibitory currents (from I→E and I→I synapses), averaged over the simulation period T [52]:

$$E/IRatio = \frac{\sum_{i=1}^{N} I_i^E(t)}{\left|\sum_{i=1}^{N} I_i^I(t)\right|}$$

where:

$I_i^E(t)$ represents excitatory synaptic currents onto neuron i at time t

$I_i^I(t)$ represents inhibitory synaptic currents onto neuron i at time t

N is the total number of neurons

$\bar{x}$ represents the mean over time T

Event synchrony (ES) quantifies spike timing coordination between excitatory neuron pairs by calculating the fraction of their spikes occurring within 5-ms windows. For each excitatory neuron pair (i, j), synchronous events are counted (with exact coincident spikes weighted by 0.5 and near-coincident spikes within the time window weighted by 1.0), then normalized by the geometric mean of both neurons' total spike counts [56]. During total simulation time T:

$$ES_{ij} = \frac{\sum_{s_i \in S_i} \sum_{s_j \in S_j} C\left(s_i, s_j\right)}{\sqrt{N_i N_j}}$$

where:
Si is the set of all spike times from neuron i during the simulation.
Sj is the set of all spike times from neuron j during the simulation.
Ni and Nj are the total number of spikes from neuron i and j respectively over the entire simulation period.
C(si, sj) counts synchronized events for each pair of spikes:

$$C\left(s_i, s_j\right) = \begin{cases} 1 & if\ 0 < |s_i - s_j| < 5ms \\ 0.5 & if\ s_i = s_j \\ 0 & otherwise \end{cases}$$

The network-wide event synchrony is computed as:

$$\text{Network ES} = \frac{1}{P} \sum_{i,j} ES_{ij}$$

Where $P = \frac{\text{Ne (Ne}-1)}{2}$ is the total number of unique excitatory neuron pairs, Ne is the number of excitatory neurons.

Both E/I ratio and ES values are normalized to baseline unpruned values to highlight pruning-induced changes in network dynamics. For statistical analysis, we conducted a correlation analysis by calculating Pearson correlation coefficients and linear regression analysis to quantify the effect sizes of excitatory and inhibitory pruning on both E/I ratio and synchronization.

3. Results

3.1 Identification and Functional Enrichment of Shared DEGs

3.1.1 Differential Expression Analysis

To reveal the shared molecular signatures underlying EP and AD models, we performed differential expression analysis using DESeq2. In the EP dataset, we

identified 378 DEGs, with 351 upregulated and 27 downregulated genes (**Fig. 1A**). The TG dataset yielded 426 progressive DEGs, including 377 upregulated and 49 downregulated genes (**Fig. 1B**). In contrast, the J20 dataset contained only one upregulated progressive DEG, Cst7 (**Fig. 1C**). Notably, 101 genes were differentially expressed in both the EP and TG datasets, representing 26.72% and 23.71% of the DEGs in each dataset, respectively (**Fig. 1A–B**). This substantial overlap suggests shared molecular pathways between EP and TG models. Detailed DEGs information is available in **Table S2**.

3.1.2 Functional Enrichment Analysis of Shared DEGs

To investigate the biological relevance of these shared DEGs between EP and TG models, we conducted a functional enrichment analysis. KEGG pathway analysis identified several most enriched pathways, including "complement and coagulation cascades," "phagosome," and "cytokine-cytokine receptor interaction" (**Fig. 1D**). GO enrichment analysis highlighted key biological processes, such as "defense response," "immune response," and "regulation of cytokine production" (**Fig. 1E**). Additionally, enriched molecular functions included "signaling receptor binding" and "immune receptor activity," with cellular components such as the "extracellular matrix" and "side of membrane" also significantly represented. These findings indicate that the shared DEGs are primarily involved in immune processes, reflecting shared molecular pathways in both EP and TG models. Detailed GO enrichment analysis results can be found in **Table S2**.

3.2 Construction of Weighted Gene Co-Expression Network

WGCNA was particularly suited for this study due to its ability to identify modules of highly correlated genes and reveal underlying biological pathways conserved across different conditions. By applying WGCNA to both EP and AD datasets, we aimed to identify conserved gene modules that may represent common molecular mechanisms between EP and AD.

After filtering out outlier samples, low-expression, and low-variance genes in each model dataset, we retained 10,997 genes common to all model datasets for further analysis (**Fig. S1A-C**). For network construction, we selected a soft-thresholding power of 9 to ensure that networks in all model datasets exhibited scale-free topology with a fit index > 0.85 (**Fig. S1D**). This threshold was consistently applied across analyses to maintain network comparability. To assess comparability between EP and AD model networks, we examined correlations of ranked mean gene expression and ranked gene connectivity between dataset pairs. For EP and J20 model datasets, high correlations were observed for both expression ($r = 0.98$, $p < 1e\text{-}200$) and connectivity ($r = 0.23$, $p < 5.7e\text{-}132$). Similarly, EP and TG model datasets showed significant correlations (expression: $r = 0.96$, $p = 1e\text{-}200$; connectivity: $r = 0.43$, $p = 1e\text{-}200$) (**Fig. S1E**), indicating comparability across model datasets [34].

We used the WGCNA package to construct gene co-expression networks for the EP, TG, and J20 model datasets. The analysis identified diverse gene modules across the three models: the EP dataset revealed 33 modules (28–790 genes per module) (**Fig. 2A**), TG had 29 modules (34–1,537 genes) (**Fig. 2B**), and J20 contained 32 modules (27–613 genes) (**Fig. 2C**). Detailed module information can be found in **Table S3**. Associations between module eigengenes (MEs) and model genotypes were assessed. The EP model dataset identified seven modules significantly associated with the EP genotype: three with positive correlations (green, steelblue, turquoise; $0.73 \leq r \leq 0.79$, $p < 3e\text{-}31$) and four with negative associations (lightyellow, red, lightcyan, paleturquoise; $-0.92 \leq r \leq -0.69$, $p < 8e\text{-}27$). Notably, five of these modules contained DEGs linked to the EP genotype (turquoise: n=198, green: n=86, steelblue: n=12, lightcyan: n=12, red: n=5) (**Fig. 2A, D**). In the TG model dataset, seven modules showed significant associations with the TG genotype: two with positive correlations (turquoise, yellow; $0.72 \leq r \leq 0.87$, $p < 3e\text{-}10$) and five with negative associations (brown, saddlebrown, darkorange2, darkmagenta, royalblue; $-0.83 \leq r \leq -0.67$, $p < 1e\text{-}08$). Nine modules contained DEGs associated with the TG genotype (turquoise: n=268, yellow: n=14, green: n=7, darkorange2: n=4, blue: n=2, orangered4: n=2, royalblue: n=2, darkmagenta: n=1, tan: n=1) (**Fig. 2B, E**). Consistent with the DEGs analysis that showed the J20 model dataset had fewer DEGs, none of the modules exhibited significant associations with the J20 genotype ($r < 0.4$) (**Fig. 2C, F**).

3.3 Module Preservation Analysis

Following module construction, we assessed the preservation of EP model modules in the AD model datasets to reveal conserve molecular pathways between EP and AD models. Our analysis revealed varying degrees of module preservation between EP and AD model datasets (**Fig. 3A-B**). In the TG model, the steelblue module had low preservation scores (Z-summary. pres = 0.89. Similarly, in the J20 model, the steelblue and yellow modules showed weak preservation (Z-summary.pres < 4), suggesting these may represent unique biological processes specific to the EP model dataset. In contrast, several EP model modules, including green, blue, and brown, exhibited high preservation scores and significant overlap with AD modules in both models, suggesting they represent conserved biological processes. Preservation statistics are shown in **Table S3**.

Notably, the turquoise EP model module had the highest preservation scores (Z-summary.pres = 83.01) and showed strong overlap with the TG model turquoise module, displaying the highest overlap counts and the lowest adjusted p-values (**Fig. 3A, C**). Both turquoise modules were positively correlated with disease genotype (EP: $r = 0.79$, $p = 5e\text{-}41$; TG: $r = 0.87$, $p = 4e\text{-}18$) and contained most DEGs in each model (**Fig. 2A, C**). Other EP modules, such as lightcyan, showed significant correlations but did not display preservation. GO enrichment analysis of this model turquoise

module revealed enrichment in immune-related terms (**Table S3**). We further assessed the preservation of the mouse turquoise module in EP and AD patient dataset (GSE63808 and GSE132903), finding that the turquoise immune modules from EP and TG models significantly overlapped with modules constructed from EP and AD patient datasets, respectively (**Fig. 3E-F, S2**). This suggests the turquoise module represents a conserved immune molecular signature across species and disease states, suggesting that immune processes play a preserved and significant role in these modules across conditions.

3.4 Shared Hub Gene Identification and Regulatory Network Analysis

To identify hub genes that may play a crucial role in both EP and AD, we intersected the hub genes of the turquoise module from EP and TG model datasets with the previously identified 101 DEGs. This analysis identified 19 shared hub genes common to both conditions (two shared hub genes not shown in the figure due to their ranking: *Apobec* and *Cxcl16*) (**Fig. 4A-B**). We then constructed a PPI network to investigate the biological significance of these 19 genes and the results showed a PPI network consisting of 14 genes **(Fig. 4C, Table S4**). This PPI network revealed strong connectivity among *C1q* complex component genes (*C1qa*, *C1qb*, *C1qc*) and other immune-related genes, including *Trem2*, *Tyrobp*, and *Adgre1*. GO biological process enrichment analysis highlighted the most significant processes involved in "Synaptic pruning" (**Fig. 4D, Table S4**). Genes involved in "Synaptic pruning" (*C1qc*, *C1qb*, *C1qa*, *Trem2*) also participate in other enriched processes, such as "Complement-mediated synapse pruning" (*C1qa*, *Trem2*) and "Microglial cell activation" (*Tyrobp*, *C1qa*, *Trem2*) (**Table S4**).

While WGCNA reveals gene co-occurrence patterns, it does not identify regulatory mechanisms. To explain potential regulatory relationships among these 19 genes, we applied the GENIE3 algorithm to gene expression profiles of the turquoise module in both EP and TG conditions (**Table S5**). By intersecting predicted regulatory networks from both conditions, we identified a shared regulatory pathway: *Tyrobp* regulates *Trem2*, which in turn regulates the complement component genes *C1q* via *C1qa* (**Fig. 4E**). These genes, particularly *Tyrobp*, *Trem2*, and *C1q* complex components gene (*C1qa*, *C1qb*, *C1qc*), play central roles in co-expression modules of both EP and TG model and are involved in multiple enriched terms, especially synaptic pruning. Notably, these genes are also progressive DEGs in the TG model (**Fig. 4F**). The successful reconstruction of a regulatory network involving *Tyrobp*, *Trem2*, and *C1q* component genes suggests they may represent a conserved molecular pathway underlying both conditions.

3.5 Validation of the Diagnostic Value of Shared Hub Genes

To further validate the clinical relevance of the identified transcriptional signatures in AD and EP animal models, we analyzed the expression of 19 shared hub genes in

datasets from AD and EP patients (GSE48350 and E-MTAB-3123) compared to controls. Thirteen of these 19 genes were expressed in both datasets, with 10 exhibiting significantly higher expression levels ($P < 0.05$) compared to controls (**Fig. 5A-B**). Notably, genes such as *Tyrobp*, *Trem2*, and *C1q* complex component genes demonstrated pronounced significance in both datasets (**Fig. 5A-B**). To assess their diagnostic potential, we developed diagnostic models leveraging the expression profiles of these genes in the hippocampus (**Fig. S2**). Using multiple machine learning methods, these models effectively differentiated disease from control groups, with particularly high performance in the EP dataset (AUC > 0.9) and satisfactory performance in the AD patient dataset (AUC > 0.7) (**Fig. S3)**. These findings confirm the diagnostic value of the transcriptional signatures identified in animal models in human AD and EP patients.

Given that these genes were shared hub genes of co-expression modules in EP and AD models, likely reflecting conserved expression pathways and progressive changes, we further examined their co-expression patterns in AD and EP patient datasets (GSE48350 and E-MTAB-3123) by calculating Pearson correlation coefficients. *Tyrobp*, *Trem2*, and the *C1q* component genes demonstrated strong correlations in both AD and EP patient datasets ($r > 0.85$), whereas co-expression patterns among other genes were less consistent across datasets (**Fig.5C-D**). Collectively, these findings suggested that synaptic pruning pathway genes such as *Tyrobp*, *Trem2*, and the *C1q* component are not only conserved between AD and EP animal models and human patients but also likely play critical roles in the underlying pathology of these conditions.

3.6 Cellular Composition Alteration and Genes Localization in Cell Type

To investigate cellular composition changes and their associations with the key hub genes (*Tyrobp*, *Trem2*, *C1q* complex genes) in TG and EP conditions, we employed CIBERSORT for cell composition deconvolution of bulk RNA-seq data. Our analysis revealed significant cellular composition alterations. Firstly, we observed a notable reduction in neuronal composition in both EP and TG conditions compared to controls ($P < 0.05$) (**Fig. 6A, C**). Secondly, there was a marked increase in microglial composition in both models ($P < 0.05$), consistent with the enrichment of immune-related processes identified in previous analyses (**Fig. 6A, C**). While astrocyte and endothelial cell alterations were also detected in EP and TG models (at 8 months, $P < 0.05$), these changes were less pronounced than the neuronal decrease and microglial increase observed in the TG model (**Fig. 6A, C**). No significant differences were found in oligodendrocyte composition in either condition.

We further examined the relationship between these cellular composition changes and the key hub genes such as *Tyrobp*, *Trem2*, and *C1q* complex genes by conducting Pearson correlation analyses (**Fig. 6B, D**). Notably, all key hub genes showed strong

negative correlations ($r < -0.7$) with neuronal composition in both EP and TG conditions, suggesting an inverse relationship between their expression levels and neuronal proportion. Conversely, strong positive correlations were observed between these genes and microglial and endothelial cell composition ($r > 0.7$). Correlations with astrocytes and oligodendrocytes were more variable and showed less consistency across genes and conditions. Although no cellular composition changes were observed in the J20 model (**Fig. S4A**), we found that genes such as *Tyrobp*, *Trem2*, and *C1q* complex components, were strongly associated with microglial composition, indicating that these genes demonstrate a strong link with microglial cell types (**Fig. S4B**). We further localized the expression of these genes to cell types using the whole mouse brain transcriptome cell type atlas from the Allen Brain Atlas [57]. The results showed that the majority (15 of 19 genes) were predominantly expressed in immune cells, particularly microglia and macrophages (**Fig. S5**).

To further explore the expression of these genes in human patient cell types, especially immune cells, we explored the expression of these genes in two large-scale sc/sn RNAseq datasets of immune cells from AD and EP patients (GSE201048 and GSE2272230) (**Fig. S6**). We found that 12 of the shared hub genes were detectable in both datasets. Among these, *Tyrobp* and *Trem2*, along with the *C1q* complex component genes, displayed notably high and predominant expression in microglia compared to other shared hub genes (**Fig. S6**). Collectively, these findings confirmed the high and predominant expression of *Tyrobp*, *Trem2*, and *C1q* components genes in the microglia of both AD and EP patients. This consistency between animal models and human patients suggests that microglia and these synaptic pruning genes play crucial roles in the progression of both AD and EP pathology and may represent a potential conserved regulatory pathway.

3.7 Computational modeling of synaptic pruning on neural network

To better understand how synaptic pruning influences neural network dynamics and its potential role in the comorbidity of AD and EP, we developed a neural network model simulating the hippocampal CA3 circuit. In this model, we systematically varied the extent of synaptic pruning (0% to 50%) at either excitatory or inhibitory synapses. We then quantified changes in the excitatory/inhibitory (E/I) ratio and synchronization levels, conducting at least 50 simulation runs per condition (**Fig. 7**).

Our findings indicate that pruning of either excitatory or inhibitory synapses alters the E/I ratio, with distinct effects. Inhibitory synaptic pruning significantly elevated the E/I ratio, while excitatory pruning reduced it. These trends were consistent across all simulations and in experiments where excitatory or inhibitory pruning was varied independently (**Fig. 7**). Correlation analysis showed a negative association between excitatory pruning and the E/I ratio ($r = -0.474$) and a positive correlation between inhibitory pruning and the E/I ratio ($r = 0.684$). Linear regression further confirmed

that excitatory pruning reduced the E/I ratio (β = -1.038), whereas inhibitory pruning increased it significantly (β = 1.454), with the effect of inhibitory pruning surpassing that of excitatory pruning.

Interestingly, inhibitory pruning displayed a moderate positive correlation with event synchronization (r = 0.346), while excitatory pruning showed only a weak negative correlation (r = −0.039) (**Fig. 7**). Linear regression analysis reflected this pattern, with inhibitory pruning exerting a stronger effect on synchronization (β = 0.358) than excitatory pruning (β = −0.041). Additionally, the E/I ratio itself was positively correlated with synchronization (r = 0.491), suggesting that the influence of synaptic pruning on network synchronization may be nonlinear and indirectly mediated by changes in the E/I balance.

These simulations suggest that excessive pruning of excitatory synapses decreases the E/I ratio and modestly suppresses network synchronization. Conversely, inhibitory pruning overpowering the effects of excitatory pruning and substantially enhancing synchronization.

4. Discussion

Alzheimer's disease (AD) and epilepsy (EP) share a complex bidirectional relationship, though the molecular pathways connecting AD-related neurodegeneration and increased EP susceptibility remain unclear. To address this issue, we used rigorous bioinformatic and computational methods to integrate and analyze transcriptional data from multiple large-scale publicly available animal models and human patient datasets. We identified consensus molecular pathways, cellular processes, and neural network dynamics associated with this comorbidity across multiple datasets.

Neuroinflammation Pathways Conserved in Epilepsy and Alzheimer's Disease

Our findings provide strong evidence supporting the hypothesis that neuroinflammatory pathways are common between AD and EP, particularly those directly triggered by tau pathology[7,19]. Differential expression analysis demonstrated significant gene overlap between EP and TG models (**Fig. 1A-B**). WGCNA revealed preservation of the immune-related turquoise module across both disease models as well as human patient datasets (**Fig. 2-3**). These results align with previous analyses of this dataset that identified significant conservation of this module across multiple AD patient cohorts [32]. We extended these findings by demonstrating the module's conservation and overlap in EP models and patient datasets, suggesting it represents a fundamental molecular pathway shared between AD and EP (**Fig. 3,5**).

Functional enrichment analysis of shared DEGs and the preserved module revealed significant enrichment in neuroinflammatory processes, including inflammatory

response, cytokine production, blood vessel morphogenesis, glial cell activation, and complement and coagulation cascades (**Fig. 1D-E, Table S3**). Additionally, we observed increased populations of neuroinflammation-associated cell types, including astrocytes, microglia, and endothelial cells, in both TG and EP animal models (**Fig. 6**).

Neuroinflammation has been extensively documented in both conditions and appears to serve a complex dual role in disease progression [58,59]. While activated microglia facilitate Aβ plaque clearance and reactive astrocytes provide metabolic support and ionic homeostasis that may attenuate neural damage and seizures, chronic activation or dysfunction of these glial populations can promote disease progression through persistent neuroinflammation [60–63]. Specifically, activated microglia and astrocytes secrete proinflammatory cytokines and chemokines, including IL-1β, TNF-α, and IL-6, which can enhance neuronal hyperexcitability, increase seizure susceptibility, exacerbate Aβ and tau aggregation, and accelerate neurodegeneration and cognitive decline [60–63] .

Additional inflammatory components, including complement cascade activation and blood-brain barrier (BBB) dysfunction, are implicated in both pathologies [64–67]. Complement activation contributes to synaptic loss in AD and is elevated in TLE patient tissue [66,67]. BBB disruption precedes neuronal hyperactivity in EP, promoting astrocyte dysfunction and seizures, while in AD it facilitates peripheral inflammatory cell infiltration, amplifying neuroinflammation [64,65].

These findings support the emerging view of neuroinflammation as a mechanistic bridge between AD and EP [19]. AD-associated inflammation can enhance neuronal hyperexcitability and seizure susceptibility. Conversely, EP-induced inflammation may accelerate Aβ and tau accumulation, contributing to cognitive decline. Our results support previous studies and suggest that neuroinflammation is highly conserved between these diseases and between species. Future studies should focus on revealing the precise causal relationship between these neuroinflammatory components and AD-EP comorbidity.

Synaptic Pruning was Identified as a Core Pathway in this Comorbidity

A comprehensive analysis of this conserved module revealed a central synaptic pruning pathway involving *Tyrobp*, *Trem2*, and *C1q* complement genes (**Fig. 4**). These genes demonstrated consistent upregulation across both AD and EP patient datasets, with preserved regulatory relationships in both animal models and human patients (**Fig. 5**). Moreover, we confirmed their specific expression in microglial cells across both animal and human patient samples (**Fig. S5-6**). Collectively, these findings suggest that microglia-mediated synaptic pruning represents a core mechanistic pathway underlying the comorbidity of AD and EP.

This pathway has been extensively characterized in AD pathology [68]. Dysregulation or mutations in *Tyrobp* and *Trem2* have established risk factors for AD through their effects on microglial function [69,70]. Under physiological conditions, microglia maintain synaptic homeostasis through a regulated process in which complement proteins, including *C1q*, tag unnecessary synapses for elimination [71]. Microglial receptors, particularly *Trem2* and *Tyrobp*, recognize these tags and initiate phagocytic clearance, a process critical for neural circuit refinement and maintenance in the adult brain [72]. In AD pathology, these receptors enable microglia to recognize protein deposits, triggering their transition to a disease-associated microglial (DAM) state characterized by enhanced phagocytic activity and elevated expression of *Tyrobp*, *Trem2*, *Apoe*, and complement proteins including *C1q* [68]. While *Tyrobp* or *Trem2* deficiency disrupts DAM activation and impairs critical microglial functions such as plaque clearance, potentially accelerating AD pathology, this pathway overactivation can also contribute to neurodegeneration and cognitive decline through excessive *C1q*-mediated synaptic pruning [68,73–75].

Synaptic pruning can exert effects on both AD and EP disease progression through two primary mechanisms: synaptic transmission and synaptic plasticity. Regarding synaptic transmission, elevated C1q expression or Aβ accumulation in the CA1 region leads to decreased miniature and evoked excitatory postsynaptic currents [76,77]. In AD, this reduction in synaptic transmission contributes to cognitive decline by disrupting normal neural communication. For EP, this alteration affects both excitatory and inhibitory neurons [78], potentially contributing to the imbalance between excitation and inhibition that characterizes epileptic activity. Notably, these effects can be reversed through C1q downregulation [79,80].

The pathway's impact on synaptic plasticity is equally significant. Research demonstrates that C1q inhibition in aged experimental models can restore both long-term potentiation (LTP) and long-term depression (LTD) [73,75,81]. In non-aged models, increased *C1q* expression also impairs the LTP process [78]. This is particularly relevant for AD, where impaired synaptic plasticity is a feature of cognitive decline. In EP, compromised synaptic plasticity may contribute to the formation and maintenance of epileptogenic circuits. The relationship between these mechanisms appears bidirectional: excessive synaptic pruning leads to neuronal damage and reduced LTP, which in turn promotes disease progression in both conditions, creating a harmful feedback loop where synaptic dysfunction promotes pathological processes.

Notably, interventions targeting this synaptic pruning pathway, either through knockdown of regulatory genes such as *Tyrobp* and *Trem2* or direct inhibition of *C1q* accumulation—have successfully restored electrophysiological level and cognitive function in AD models, even in the presence of significant amyloid and tau pathology

[68,73–75]. Our results establish a regulatory network that is consistent with previous observations and further extends its role in the comorbidity of AD and EP (**Fig. 4**).

While this pathway is extensively studied in the context of AD, to the best of our knowledge, no prior research has established a connection between this pathway and the comorbidity of EP and AD. Our understanding of the relationship between synaptic pruning and EP remains nascent, especially how to interpret its contribution to the network dynamics [82]. To address this gap, we conducted an in-silico experiment to shed light on this issue.

Synaptic Pruning Alter E/I Balance to Promote Network Synchronization

Computational modeling has become an important tool for understanding AD and EP pathology, models ranging from molecular-level simulations of ion dynamics to large-scale network models [83,84]. Disruption of excitatory/inhibitory (E/I) balance and neural synchronization represent a key point of convergence between AD and EP pathology, supported by a wealth of experimental evidence. In EP, patch-clamp recordings show reduced GABAergic inhibition and enhanced glutamatergic transmission, leading to network hyperexcitability [85,86]. In AD, studies have shown that AD mouse models exhibit spontaneous epileptiform activity, while human studies using magnetoencephalography have demonstrated disruption of synchronization in multiple frequency bands [16,87].

To explore how synaptic pruning contributes to the comorbidity of AD and EP, we developed a computational model of the hippocampal CA3 circuit on top of Liu's biologically plausible EP modeling. We calibrate fixed synaptic strength by adjusting conductance-based synapses to produce realistic EPSPs/IPSPs based on animal experiments. [16,87], while leveraging synaptic connection pruning across simulation trials on independently standard normal synaptic weights to transition the network into abnormal states. This model allowed us to quantify how pruning of excitatory and inhibitory synapses affects E/I balance (E/I ratio) and the temporal coordination of neural firing (synchronization) [86].

Our computational model suggests that synaptic pruning can regulate the E/I balance in neural networks, with inhibitory synapse pruning having a more pronounced effect. Quantitative analysis by linear regression showed that excitatory synapse elimination decreased the E/I ratio ($\beta = -1.038$), while inhibitory synapse removal led to a large increase in the E/I ratio ($\beta = 1.454$) (**Fig. 7**). Our finding that inhibitory pruning has a stronger (enhancing) effect on network dynamics can be explained by the function of inhibitory interneurons within neural circuits. These neurons often establish synaptic connections with multiple excitatory neurons and act as regulators of circuit coordination and synchronization [88]. Therefore, when inhibitory control mechanisms are impaired, the resulting disruption of regulation will trigger dysregulation that

extends to more widespread circuits. Moreover, endogenous homeostatic mechanisms such as synaptic scaling appear to have a limited capacity to compensate for the loss of inhibitory synapses [89]. Ultimately, a reduction in inhibitory synapses may produce a larger perturbation in neural networks than an equivalent reduction in excitatory synapses.

Interestingly, our findings reveal a weaker correlation of synaptic pruning on network synchronization compared to its impact on the E/I ratio. Specifically, inhibitory pruning exhibited a moderate positive correlation with synchronization (r=0.346), whereas excitatory pruning had a negligible correlation (r=−0.039). Notably, the E/I ratio itself demonstrated a strong correlation with synchronization levels (r=0.491). While it seems intuitive that enhancing network excitability can enhance synchrony, the results of our analysis predict the importance of considering the specific location and functional role of pruned synapses in neural circuits [88]. For instance, in a circuit that has an inhibitory effect on the broader network, pruning synapses that inhibit this circuit will paradoxically reduce network synchronization. This explains the indirect, nonlinear association of synaptic pruning with network synchronization, as shown in our results (**Fig. 7**). Our results suggest that the importance of synaptic pruning for comorbid phenomena in EP and AD requires consideration of the regional, structural, and functional context of pruning.

Importantly, our computational model emphasizes this inhibitory synaptic pruning role aligns with previous observations on this microglial synaptic pruning pathway [90]. Studies have shown that the *Trem2-C1q* microglial synaptic pruning pathway preferentially targets inhibitory synapses in AD, while recent research demonstrates similar preferential pruning of inhibitory synapses during recurrent seizures that exacerbate EP pathology [90,91]. Our modeling results reflect this preferential pruning of inhibitory synapses in AD and EP and further suggest that at the network level, this process favors E/I balance toward excitatory, further promoting network synchronization that can lead to epileptic outcomes (**Fig. 7**). At the molecular level, *C1q* acts as an "eat me" signal, tagging synapses for microglia to eliminate [82]. While this tagging process is not synapse-type specific, microglia demonstrate selective pruning of inhibitory synapses [82,90]. Studies have shown that *C1q* blockade reduces both the frequency and severity of seizures in traumatic brain injury models [92]. However, it is also important to note that *C1q* knockout also affects synaptic elimination during development, resulting in enhanced connectivity and seizure activity [93,94]. These findings suggest the importance of managing microglial *C1q*-mediated synaptic pruning during AD pathology and aging. Mendelian randomization studies have also found that *C1qa* is a risk factor for AD and EP (**Fig. S7**). In fact, in AD, synaptic loss often precedes cognitive decline and EP, which suggests that it may be an initiating event rather than a consequence [95].

Overall, our analysis and computational modeling support the hypothesis that persistent activation of complement-mediated synaptic elimination may disproportionately affect inhibitory synapses, shifting the E/I balance toward excitation and potentially promoting seizure activity [82,85]. We further demonstrate how the above pathway plays a role in the comorbidity of AD and EP and propose a plausible framework (**graphic abstract**): The accumulation of amyloid plaques and tau tangles in AD triggers microglial activation into a DAM state, characterized by elevated expression of phagocytic and inflammatory genes, particularly *Tyrobp* and *Trem2*. These proteins recognize neuronal damage and initiate microglial recruitment for debris clearance and synaptic pruning through complement proteins such as *C1q*. While this process is designed to reduce plaque burden and maintain neural circuit integrity, the preferential pruning of inhibitory synapses by microglia disrupts the E/I balance that increase network excitability to induce seizures, which can further aggravate inflammation and protein aggregation.

Future research and limitations

Our study has two limitations: while our analysis mined a conserved microglial synaptic pruning pathway across multiple datasets, we primarily relied on bulk RNAseq data that cannot fully capture cell subtype specificity. Although we attempted to address this limitation through computational deconvolution and validation of single-cell datasets, future studies should employ spatial transcriptomic approaches to advance understanding of the cell subtype-specific contribution to AD-EP comorbidity, for example, by tracking changes in microglial activation patterns and synaptic action in AD and EP. In addition, while our computational model provides insights into the contribution of synaptic pruning to network dynamics, it simplifies many aspects of real neural circuits, such as topology, cell types, and dendritic details within neural circuits. Future models could incorporate more detailed cellular mechanisms to better reflect the progression of AD and EP comorbidity at the molecular level.

Figures and legends

Figure 1: Differential Expression and Functional Enrichment Analyses in EP and AD Model Datasets

(A) Volcano plot shows the DEGs in the EP model dataset. The x-axis represents the log2 fold change, and the y-axis shows the -log10 adjusted p-value. Upregulated genes are highlighted in red, and downregulated genes are in blue. The dashed lines mark the thresholds for significance (adjusted p-value < 0.05 and |log2 fold change| > 1). **(B)** Differential expression analysis of the TG model dataset. Scatter plot showing progressive DEGs identified across different ages (4, 6, and 8 months) compared to their control and initial months. DEGs are color-coded based on their expression level (log2 fold change) compared to the control and initial month, with dot size to show significance (adjusted p-value). The shaded regions correspond to the different age groups, with the numbers indicating the count of EP-DEGs (numerator) and total

DEGs (denominator) with a log2 fold change below 1 that marks the threshold for non-significant genes. **(C)** The single upregulated progressive DEG, Cst7, detected in the J20 model dataset across different ages (6, 8, 10, and 12 months). The plot shows the expression level of *Cst7* over time (x-axis: Age in months; y-axis: Normalized counts), with different genotypes (J20 and WT) represented by different colors. Dashed lines represent mean paths for each age. (LRTstatistic=43.70, log2foldchange[6-12months] = 2.73, FDR=2.91E-5). **(D)** KEGG pathway enrichment analysis of shared DEGs between the EP and TG datasets. The bubble plot indicates the significantly enriched pathways, with bubble size representing the gene count and color indicating the significance level (-log10 adjusted p-value). **(E)** GO enrichment analysis of shared DEGs between the EP and TG model datasets. The dot plot shows the enriched biological processes (BP), cellular components (CC), and molecular functions (MF). Dot size corresponds to gene count, while color represents the significance level (-log10 adjusted p-value). Immune-related functions were prominently enriched.

Figure 2: Co-Expression Network Construction and Model-Trait Association

(A-C) Hierarchical clustering dendrograms are presented for the EP (**A**), TG (**B**), and J20 (**C**) model datasets, with gene modules identified through dynamic tree cutting. The colors in the heatmap below each dendrogram correspond to distinct gene modules, where the clustering of similar colors between the EP and other model datasets (TG and J20) reflects the conservation of modules across conditions. The GS is shown with darker colors indicating stronger correlations: red represents positive correlations, and blue represents negative correlations with disease genotypes (EP for panel A, TG for panel B, and J20 for panel C). Overlapping red areas in the module-trait relationships suggest that these modules may be positively correlated with both EP and AD model, as seen in the turquoise module in the TG model dataset. The DEG row shows the distribution of DEGs within the modules: red indicates DEGs, while grey indicates non-DEGs. **(D-F)** Heatmaps of the module-trait relationships in EP (**D**), TG (**E**), and J20 (**F**) model datasets. The heatmaps show the Pearson correlation coefficients between MEs and genotypes. The color scale represents the strength and direction of the correlation, with red indicating positive and blue indicating negative correlations. Modules are considered as significant association with genotype using threshold (p-value < 0.05, |r| > 0.65).

Figure 3: Module Preservation Analysis Across EP and AD Datasets

(A, B) Zsummary preservation statistics of EP model modules in the TG and J20 model datasets, respectively. Each point represents an EP model module, with the y-axis displaying the Zsummary preservation statistic. A Zsummary > 10 indicates strong evidence of preservation, 2 < Zsummary < 10 indicates moderate evidence, and Zsummary < 2 suggests no evidence of preservation. The gray horizontal line at Z=10 and the black horizontal line at Z=2 serve as reference points in the plots. The module

size is indicated by the x-axis, and the color represents the module color. **(C, D)** Bubble plots show the cross-tabulation of EP model modules with TG (**C**) and J20 (**D**) model modules; the cross-tabulation of EP patient (GSE63808) and EP model datasets (**E**); cross-tabulation of AD (GSE132903) and TG mouse model datasets (**F**). The color scale represents the adjusted p-value for the overlap significance, while the size of the dots corresponds to the number of overlapping genes. Larger, more significant dots indicate stronger overlaps between EP and AD modules such as the turquoise module. Only significantly overlapping with overlap count > 30 and adjusted p-value < 0.05 was colored, while those with insignificant overlap are marked in gray.

Figure 4: Identification and Network Analysis of Shared Hub Genes in EP and AD Datasets

(**A**) Network plot illustrating the top 50 genes within the conserved turquoise module across both the EP and TG datasets. Each node represents a gene, and edges signify gene co-expression connections. Grey edges correspond to connections in the EP dataset, while blue edges represent those in the TG dataset. The color of the nodes indicates their level of connectivity, with deeper color, indicating higher connectivity within the network such as *Capg*, *Msn*, and *Npc2*. 17 red nodes are shared hub genes that exhibit high connectivity in both networks and are identified as DEGs under both conditions. Two shared hub genes are not shown in the figure due to their ranking in both modules: *Apobec* and *Cxcl16*. (**B**) Venn diagram depicting the overlap between hub genes identified in the EP and AD datasets and shared DEGs. 19 shared hub genes were identified as key drivers in both conditions. (**C**) PPI network of the 14 shared hub genes constructed from 19 shared hub genes using the STRING database. The size and color of the nodes are colored by their connectivity in the PPI network. (**D**) The bubble plot showed the top GO biological process enrichment terms based on p-values for the 19 shared hub genes. (**E**) The shared gene regulatory network was inferred using the GENIE3 algorithm, showing the regulatory relationships among the shared hub genes. (**F**) Progressive upregulation of key 5 shared hub genes involved in microglial synaptic pruning across different ages in the TG mouse model. The plot shows the expression level of these genes over time (x-axis: Age in months; y-axis: Normalized counts), with different genotypes represented by different colors (WT: black, TG: teal). Dashed lines represent mean paths for each age. LRT statistics of these genes can be found in **Table S2**.

Figure 5. Expression analysis and correlation patterns of shared hub genes in AD and EP patient datasets

(**A, B**) Violin plots showing the differential expression of shared hub genes between control and disease groups in (**A**) EP patient dataset (E-MTAB-3123) and (**B**) AD patient dataset (GSE48350). Red violins represent control groups and blue violins represent disease groups. The width of each violin indicates the density of data points, and the internal box plots show the median and interquartile ranges. The Wilcoxon

p-value is shown for each comparison. (**C, D**) Correlation heatmap showing the relationships between shared hub genes and age in the EP patient dataset (E-MTAB-3123) and AD patient dataset (GSE48350). The color intensity and box size represent the strength of Pearson correlation coefficients (r), with red indicating positive correlations and blue indicating negative correlations

Figure 6: Cellular Composition Deconvolution and Association with Shared Hub Genes in EP and TG Datasets

(**A, C**) The plot shows the estimated proportions of different cell types (astrocytes, neurons, oligodendrocytes, microglia, and endothelial) in control and EP model conditions (**A**), and TG model condition (**C**). The x-axis represents different conditions or months, and the y-axis shows the proportions of specific cell types in each condition, with different genotypes represented by different colors. The Mann-Whitney test was performed to determine significant cell composition difference ($P < 0.05$) in EP model dataset. The Kruskal-Wallis test was performed to determine the significance ($q < 0.05$) with the BH method was used to adjust the P-value in pairwise comparisons among different groups in the TG model dataset. (**B, D**) Correlation heatmap showing the relationships between key shared hub genes and cell composition in the EP model dataset. The color intensity represents the strength of Pearson correlation coefficients (r), with red indicating positive correlations and blue indicating negative correlations. The significance of correlations with shared hub gene is shown by red arrows, with arrow color proportional to correlation strength.

Figure 7. Effects of excitatory and inhibitory synaptic pruning on neural network dynamics

Three-dimensional scatter plot showing the relationship between excitatory pruning ratio (0-0.5), inhibitory pruning ratio (0-0.5), and normalized E/I ratio. Each dot presents a simulation result. Colors indicate normalized synchronization levels from blue (lower), and white (no change) to red (higher).

Legends of supplementary files

Table S1: Summary of Quality Control and Mapping Statistics for Bulk RNA-seq Samples

Detailed summary of the QC and mapping statistics for all RNA-seq samples analyzed in this study. For each sample, the total number of raw reads, the number of reads passing quality filtering through Fastp, and the reads retained after rRNA contamination removal by ribodetector are reported. Each sample is categorized by the experimental group, including relevant age and condition tags, and further classified into either the AD or EP dataset. Notes regarding any specific issues or annotations on individual samples are also provided.

Table S2: Differential Expression and Functional Enrichment Analysis of Shared DEGs

Summary of differential expression and functional enrichment analyses across three datasets: EP, TG, and J20 mouse models.

Table S3: Module Construction, Preservation, and Functional Enrichment of Gene Co-Expression Networks in Mouse Models

Summary of WGCNA on EP, TG, and J20 mouse models. The table is divided into multiple sections, including the gene modules' membership identified in each dataset and their correlations with model-specific genotypes. Additionally, module preservation analyses between the EP and AD datasets are included. GO enrichment analyses of the turquoise modules are also shown.

Table S4: Protein-Protein Interaction Network and GO Biological Process Enrichment Analysis of Shared Hub Genes.

Analysis results of the PPI network constructed for 19 shared hub genes identified across EP and TG models. The table is divided into three sections. The PPI GO sheet summarizes the results of the GO biological process enrichment analysis. The PPI Degree sheet lists each gene and its degree of connectivity within the network. The PPI Interaction sheet details the specific interactions between these genes.

Table S5: Regulatory Network Prediction Using GENIE3 for Turquoise Module in Mice Models

Results of regulatory network inference were conducted using the GENIE3 machine learning algorithm on the gene expression profiles of the turquoise module from the EP) and TG models. The table is divided into two sections: GENIE3TG and GENIE3EP, representing the predicted regulatory relationships within the TG and EP datasets, respectively. Each section lists the regulatory gene, the target gene, and the corresponding weight of the predicted regulatory interaction.

Table S6: Cell Composition Deconvolution of Bulk RNA-seq Data

Results of cell composition deconvolution analysis conducted using CIBERSORT from BrainDeconvShiny on bulk RNA-seq data from the EP and AD models. The table includes the estimated proportions of major brain cell types, including neurons, astrocytes, oligodendrocytes, microglia, and endothelial for each sample, alongside the sample identifiers, group classification, age, and condition type (e.g., rTg4510, Wild Type).

Figure S1. Construction of co-expression module in model datasets

(**A-C**) Hierarchical clustering dendrograms and trait heatmaps for the EP, rTg4510, and J20 datasets. (**A**) EP dataset, (**B**) rTg4510 dataset, and (**C**) J20 dataset. Hierarchical clustering was performed on variance-stabilized gene expression data to

identify potential outliers. The top 85% of genes with the highest Median Absolute Deviation (MAD) were retained, and outliers were detected and removed before network construction. Two samples were removed from the rTg4510 dataset, and three samples were removed from the J20 dataset. The heatmaps below each dendrogram display the trait data associated with each sample, with red indicating outliers or specific traits of interest. **(D-F)** Soft-thresholding power Selection and Comparability Assessment, **(D)** Selection of the soft-thresholding power for network construction. The left panel shows the scale-free topology fit index (y-axis) as a function of the soft-thresholding power (x-axis) for EP, TG, and J20 datasets. The right panel depicts the mean connectivity (y-axis) against soft-thresholding power, indicating that a power of 9 was chosen for all datasets to achieve scale-free topology with $R^2 > 0.85$. **(F)** Comparability assessment of the EP, TG, and J20 datasets. Scatter plots display the correlations between ranked mean gene expression (top) and ranked gene connectivity (bottom) between EP and TG datasets (left) and between EP and J20 datasets (right). Positive correlations and significant P values suggest strong comparability between datasets.

Figure S2. Construction of co-expression module in patient datasets

(**A**) Scale independence and mean connectivity plots across soft-thresholding powers for the EP (GSE63808) and AD (GSE132903) patient datasets, with a selected soft-thresholding power of 9 ensuring a scale-free topology ($R^2 \geq 0.85$). (**B-C**) Dendrogram of gene modules identified in the EP and AD dataset using hierarchical clustering and dynamic tree cutting based on topological overlap matrices (TOM).

Figure S3: ROC curve of Diagnostic model

(**A**) in EP patient dataset (E-MTAB-3123) and (**B**) in AD patient dataset (GSE48350). ROC curves of various machine learning classifiers in classifying disease cases from control participants based on selected gene expression data. Remarkably, most of the models have an AUC between 0.85 and 0.92 in EP patient dataset, with the best performance recorded with XGBoost, reaching the highest AUC score in this EP dataset (AUC=0.92). Although the AD model diagnostic efficiency is not as high as that of the EP dataset, which may reflect the complex disease background of AD, these diagnostic models still show high diagnostic efficiency (AUC>0.7).

Figure S4: Cellular Composition Deconvolution and Association with Shared Hub Genes in J20 Datasets

(**A**) The plot shows the cell composition level over time in J20 dataset (x-axis: Age in months; y-axis: Normalized counts), with different genotypes represented by different colors (WT: black, J20: teal). Dashed lines represent mean paths for each age. The Kruskal-Wallis test was performed to determine the significance with the BH method was used to adjust the P-value in pairwise comparisons among different groups, with a significance level of $q < 0.05$. (**B**) Correlation heatmap showing the relationships

between key shared hub genes and cell composition in the J20 model dataset. The color intensity represents the strength of Pearson correlation coefficients (r), with red indicating positive correlations and blue indicating negative correlations.

Figure S5: Expression Localization of Shared Hub Genes in Mouse Brain Cell Types Using the Whole Mouse Brain Transcriptomic Cell Type Atlas

This figure shows the expression patterns of 19 shared hub genes across various cell types in the mouse brain, based on the Whole Mouse Brain Transcriptomic Cell Type Atlas (https://assets.nemoarchive.org/dat-qg7n1b0) from the Allen Brain Cell Atlas. The top left panel illustrates the localization and color of various cell types, such as astrocytes, microglia, macrophages, endothelial cells, and oligodendrocytes in the brain atlas. Each circular panel highlights the specific expression profile of one gene, with darker shading representing higher expression levels. Most of these genes (15 out of 19) are predominantly expressed in immune cells, specifically microglia and macrophages.

Figure S6: Single-cell and Single-nucleus RNA Sequencing Analysis of Hub Gene Expression in Immune Cells of Epilepsy and Alzheimer's Disease Patients

(**A, D**) Dot plot displaying the expression of shared hub genes across different identified cell types in the EP patient dataset. The size of the dots represents the proportion of cells expressing each gene, and the color intensity indicates the average expression level. (**A**) EP patient dataset (GSE227223), (**D**) AD patient dataset (GSE201048). (**B, E**) t-SNE plot showing the clustering of cells in the EP and AD dataset based on their gene expression profiles, with distinct colors representing different cell types. (**B**) EP dataset, (**E**) AD dataset. (**C, F**) Feature plots showing the expression patterns of individual hub genes within the EP dataset, over on the t-SNE map. Darker purple areas represent higher expression levels. *TYROBP*, *TREM2*, *C1QA*, *C1QB*, and *C1QC* exhibit high expression predominantly in microglia clusters. (C) EP dataset, (F) AD dataset.

Figure S7: Forest plot of Mendelian randomization result from DMRdb

Forest plot showing hazard ratios (HR) and 95% confidence intervals (CI) for associations between Alzheimer's disease subtypes, epilepsy, and *C1QA* http://www.inbirg.com/DMRdb/. Red dots represent point estimates for hazard ratios, and horizontal lines indicate 95% confidence intervals. P-values are shown for each association. Values greater than 1.0 indicate increased risk for the outcome.

Data and code availability

All sequencing and microarray data used in this study are publicly accessible through the National Center for Biotechnology Information (NCBI) or European Nucleotide Archive (ENA) under the following accession numbers: PRJEB18790, GSE125957, GSE48350, E-MTAB-3123 GSE63808, GSE132903, GSE201048, and GSE227223.

The code supporting the analyses is available at https://github.com/HuihongLi/AD-EP-MS-Code. Additional data can be provided upon reasonable request to the corresponding authors.

CRediT authorship contribution statement

Huihong Li: Conceptualization, Investigation, Methodology, Writing – original draft, Writing – review & editing, Formal analysis.
Zhiran Xie: Investigation, Formal analysis, Writing – original draft, Writing – review & editing
Yuxuan Tian: Investigation, Formal analysis, Writing – original draft, Writing – review & editing
Bingying Lin: Investigation, Writing – review & editing
Jianwei Li: Writing – original draft, Writing – review & editing
Jie Wu: Conceptualization, Writing – original, Writing – review & editing
Mingjie Chen: Investigation, Writing – review & editing
Xueke Liu: Investigation, Writing – review & editing
Yushan Sun: Investigation, Writing – review & editing
Si Chen: Writing – review & editing
Zihan Deng: Writing – review & editing
Mengqi Hong: Writing – review & editing
Bing Huang: Conceptualization, Writing – original draft, Writing – review & editing
Naili Wei: Conceptualization, Writing – original draft, Writing – review & editing
Xiaoyu Ji: Conceptualization, Supervision, Funding acquisition, Writing – original, Writing – review & editing

Funding statement
This research was supported by the Young Scientists Fund of the National Natural Science Foundation of China (Grant Nos. 82201629) and the Guangdong Provincial Science and Technology Special Fund (Grant Nos. 210803136872196)

Declaration of Competing Interest
The authors declare that they have no known competing financial interests or personal relationships that could have appeared to influence the work reported in this paper.

Acknowledgments
We thank our lab members for engaging in discussions and improving the manuscript.

References:
1. Giorgi, F. S., Saccaro, L. F., Busceti, C. L., Biagioni, F. & Fornai, F. Epilepsy and Alzheimer's Disease: Potential mechanisms for an association. *Brain*

Research Bulletin vol. 160 Preprint at https://doi.org/10.1016/j.brainresbull.2020.04.009 (2020).

2. Kamondi, A., Grigg-Damberger, M., Löscher, W., Tanila, H. & Horvath, A. A. Epilepsy and epileptiform activity in late-onset Alzheimer disease: clinical and pathophysiological advances, gaps and conundrums. *Nature Reviews Neurology* vol. 20 Preprint at https://doi.org/10.1038/s41582-024-00932-4 (2024).
3. Fang, Y. *et al*. Alzheimer Disease and Epilepsy: A Mendelian Randomization Study. *Neurology* **101**, (2023).
4. Wimo, A., Jönsson, L., Bond, J., Prince, M. & Winblad, B. The worldwide economic impact of dementia 2010. *Alzheimer's and Dementia* **9**, (2013).
5. Ngugi, A. K., Bottomley, C., Kleinschmidt, I., Sander, J. W. & Newton, C. R. Estimation of the burden of active and life-time epilepsy: A meta-analytic approach. *Epilepsia* **51**, (2010).
6. Mendez, M. F. & Lim, G. T. H. Seizures in elderly patients with dementia: Epidemiology and management. *Drugs Aging* **20**, (2003).
7. Leitner, D. *et al*. Similar brain proteomic signatures in Alzheimer's disease and epilepsy. *Acta Neuropathol* **147**, (2024).
8. Pandis, D. & Scarmeas, N. Seizures in Alzheimer Disease: Clinical and Epidemiological Data. *https://doi.org/10.5698/1535-7511-12.5.184* **12**, 184–187 (2012).
9. Tombini, M. *et al*. Temporal Lobe Epilepsy and Alzheimer's Disease: From Preclinical to Clinical Evidence of a Strong Association. *Journal of Alzheimer's Disease Reports* vol. 5 Preprint at https://doi.org/10.3233/ADR-200286 (2021).
10. Johnson, E. L. *et al*. Association between Midlife Risk Factors and Late-Onset Epilepsy: Results from the Atherosclerosis Risk in Communities Study. *JAMA Neurol* **75**, (2018).
11. Stefanidou, M. *et al*. Bi-directional association between epilepsy and dementia: The Framingham Heart Study. *Neurology* **95**, (2020).
12. Gourmaud, S. *et al*. Alzheimer-like amyloid and tau alterations associated with cognitive deficit in temporal lobe epilepsy. *Brain* **143**, (2020).
13. Tai, X. Y. *et al.* Hyperphosphorylated tau in patients with refractory epilepsy correlates with cognitive decline: A study of temporal lobe resections. *Brain* **139**, (2016).
14. Zou, Y. *et al.* Epileptic seizures induced by pentylenetetrazole kindling accelerate Alzheimer-like neuropathology in 5×FAD mice. *Front Pharmacol* **15**, 1500105 (2024).
15. Watts, M. E., Pocock, R. & Claudianos, C. Brain energy and oxygen metabolism: Emerging role in normal function and disease. *Front Mol Neurosci* **11**, 396508 (2018).
16. Born, H. A. Seizures in Alzheimer's disease. *Neuroscience* **286**, 251–263 (2015).

17. Toniolo, S., Sen, A. & Husain, M. Modulation of Brain Hyperexcitability: Potential New Therapeutic Approaches in Alzheimer's Disease. *International Journal of Molecular Sciences 2020, Vol. 21, Page 9318* **21**, 9318 (2020).
18. Kalyvas, A. C., Dimitriou, M., Ioannidis, P., Grigoriadis, N. & Afrantou, T. Alzheimer's Disease and Epilepsy: Exploring Shared Pathways and Promising Biomarkers for Future Treatments. *Journal of Clinical Medicine 2024, Vol. 13, Page 3879* **13**, 3879 (2024).
19. Liew, Y. *et al.* Neuroinflammation: A Common Pathway in Alzheimer's Disease and Epilepsy. *Journal of Alzheimer's Disease* **94**, S253–S265 (2023).
20. Targa Dias Anastacio, H., Matosin, N. & Ooi, L. Neuronal hyperexcitability in Alzheimer's disease: what are the drivers behind this aberrant phenotype? *Translational Psychiatry 2022 12:1* **12**, 1–14 (2022).
21. Bele, T. & Ingale, S. Network-based investigation to identify the common gene-disease linkage between Alzheimer's disease, Parkinson's disease, and epilepsy. *Network Biology* **2024**, 254–265.
22. Mao, R. *et al.* Impairments of GABAergic transmission in hippocampus mediate increased susceptibility of epilepsy in the early stage of Alzheimer's disease. *Cell Communication and Signaling* **22**, 1–16 (2024).
23. Barker-Haliski, M. & Steve White, H. Glutamatergic Mechanisms Associated with Seizures and Epilepsy. *Cold Spring Harb Perspect Med* **5**, a022863 (2015).
24. Tang, Y., Yan, Y., Mao, J., Ni, J. & Qing, H. The hippocampus associated GABAergic neural network impairment in early-stage of Alzheimer's disease. *Ageing Res Rev* **86**, 101865 (2023).
25. Bosco, F. *et al.* Antiseizure Medications in Alzheimer's Disease from Preclinical to Clinical Evidence. *International Journal of Molecular Sciences 2023, Vol. 24, Page 12639* **24**, 12639 (2023).
26. Andrews, S. FastQC. *Babraham Bioinformatics* (2010).
27. Chen, S., Zhou, Y., Chen, Y. & Gu, J. Fastp: An ultra-fast all-in-one FASTQ preprocessor. in *Bioinformatics* vol. 34 (2018).
28. Deng, Z. L., Münch, P. C., Mreches, R. & McHardy, A. C. Rapid and accurate identification of ribosomal RNA sequences via deep learning. *Nucleic Acids Res* **50**, (2022).
29. Kim, D., Paggi, J. M., Park, C., Bennett, C. & Salzberg, S. L. Graph-based genome alignment and genotyping with HISAT2 and HISAT-genotype. *Nat Biotechnol* **37**, (2019).
30. Liao, Y., Smyth, G. K. & Shi, W. FeatureCounts: An efficient general purpose program for assigning sequence reads to genomic features. *Bioinformatics* **30**, (2014).
31. Love, M. I., Huber, W. & Anders, S. Moderated estimation of fold change and dispersion for RNA-seq data with DESeq2. *Genome Biol* **15**, (2014).
32. Castanho, I. *et al.* Transcriptional Signatures of Tau and Amyloid

Neuropathology. *Cell Rep* **30**, (2020).
33. Elizarraras, J. M. *et al.* WebGestalt 2024: faster gene set analysis and new support for metabolomics and multi-omics. *Nucleic Acids Res* **52**, W415–W421 (2024).
34. Miller, J. A., Horvath, S. & Geschwind, D. H. Divergence of human and mouse brain transcriptome highlights Alzheimer disease pathways. *Proc Natl Acad Sci U S A* **107**, (2010).
35. Langfelder, P. & Horvath, S. WGCNA: An R package for weighted correlation network analysis. *BMC Bioinformatics* **9**, (2008).
36. Zhang, B. & Horvath, S. A general framework for weighted gene co-expression network analysis. *Stat Appl Genet Mol Biol* **4**, (2005).
37. Ritchie, M. E. *et al.* Limma powers differential expression analyses for RNA-sequencing and microarray studies. *Nucleic Acids Res* **43**, (2015).
38. Schober, P. & Schwarte, L. A. Correlation coefficients: Appropriate use and interpretation. *Anesth Analg* **126**, (2018).
39. Langfelder, P., Luo, R., Oldham, M. C. & Horvath, S. Is my network module preserved and reproducible? *PLoS Comput Biol* **7**, (2011).
40. Szklarczyk, D. *et al.* The STRING database in 2023: protein-protein association networks and functional enrichment analyses for any sequenced genome of interest. *Nucleic Acids Res* **51**, (2023).
41. Huynh-Thu, V. A., Irrthum, A., Wehenkel, L. & Geurts, P. Inferring regulatory networks from expression data using tree-based methods. *PLoS One* **5**, (2010).
42. Newman, A. M. *et al.* Robust enumeration of cell subsets from tissue expression profiles. *Nat Methods* **12**, (2015).
43. Sutton, G. J. *et al.* Comprehensive evaluation of deconvolution methods for human brain gene expression. *Nat Commun* **13**, (2022).
44. Robinson, M. D., McCarthy, D. J. & Smyth, G. K. edgeR: A Bioconductor package for differential expression analysis of digital gene expression data. *Bioinformatics* **26**, (2009).
45. Zhang, Y. *et al.* An RNA-sequencing transcriptome and splicing database of glia, neurons, and vascular cells of the cerebral cortex. *Journal of Neuroscience* **34**, (2014).
46. Hao, Y. *et al.* Dictionary learning for integrative, multimodal and scalable single-cell analysis. *Nat Biotechnol* **42**, (2024).
47. Kumar, P. *et al.* Single-cell transcriptomics and surface epitope detection in human brain epileptic lesions identifies pro-inflammatory signaling. *Nat Neurosci* **25**, (2022).
48. Sun, N. *et al.* Human microglial state dynamics in Alzheimer's disease progression. *Cell* **186**, (2023).
49. Stimberg, M., Brette, R. & Goodman, D. F. M. Brian 2, an intuitive and efficient neural simulator. *Elife* **8**, (2019).
50. Izhikevich, E. M. Simple model of spiking neurons. *IEEE Trans Neural Netw*

14, 1569–1572 (2003).

51. Tzavellas, N. P. *et al.* Firing Alterations of Neurons in Alzheimer's Disease: Are They Merely a Consequence of Pathogenesis or a Pivotal Component of Disease Progression? *Cells* vol. 13 Preprint at https://doi.org/10.3390/cells13050434 (2024).
52. Sammons, R. P. *et al.* Structure and function of the hippocampal CA3 module. *Proc Natl Acad Sci U S A* **121**, (2024).
53. Vyleta, N. P., Borges-Merjane, C. & Jonas, P. Plasticity-dependent, full detonation at hippocampal mossy fiber-CA3 pyramidal neuron synapses. *Elife* **5**, (2016).
54. Liu, Y., Grigorovsky, V. & Bardakjian, B. Excitation and Inhibition Balance Underlying Epileptiform Activity. *IEEE Trans Biomed Eng* **67**, (2020).
55. Penn, Y., Segal, M. & Moses, E. Network synchronization in hippocampal neurons. *Proc Natl Acad Sci U S A* **113**, (2016).
56. Yao, Z. *et al.* A high-resolution transcriptomic and spatial atlas of cell types in the whole mouse brain. *Nature* **624**, (2023).
57. Vezzani, A., French, J., Bartfai, T. & Baram, T. Z. The role of inflammation in epilepsy. *Nature Reviews Neurology 2010 7:1* **7**, 31–40 (2010).
58. Heneka, M. T., Golenbock, D. T. & Latz, E. Innate immunity in Alzheimer's disease. *Nature Immunology 2015 16:3* **16**, 229–236 (2015).
59. Pekny, M. & Pekna, M. Astrocyte reactivity and reactive astrogliosis: Costs and benefits. *Physiol Rev* **94**, (2014).
60. Chen, Z. P. *et al.* Lipid-accumulated reactive astrocytes promote disease progression in epilepsy. *Nat Neurosci* **26**, (2023).
61. Onyango, I. G., Jauregui, G. V, Čarná, M., Bennett, J. P. & Stokin, G. B. Neuroinflammation in Alzheimer's disease. *Biomedicines* vol. 9 Preprint at https://doi.org/10.3390/biomedicines9050524 (2021).
62. Vezzani, A. & Viviani, B. Neuromodulatory properties of inflammatory cytokines and their impact on neuronal excitability. *Neuropharmacology* **96**, 70–82 (2015).
63. van Vliet, E. A., Aronica, E. & Gorter, J. A. Blood-brain barrier dysfunction, seizures and epilepsy. *Seminars in Cell and Developmental Biology* vol. 38 Preprint at https://doi.org/10.1016/j.semcdb.2014.10.003 (2015).
64. Zlokovic, B. V. Neurovascular pathways to neurodegeneration in Alzheimer's disease and other disorders. *Nature Reviews Neuroscience* vol. 12 Preprint at https://doi.org/10.1038/nrn3114 (2011).
65. Kopczynska, M. *et al.* Complement system biomarkers in epilepsy. *Seizure* **60**, (2018).
66. Veerhuis, R., Nielsen, H. M. & Tenner, A. J. Complement in the brain. *Molecular Immunology* vol. 48 Preprint at https://doi.org/10.1016/j.molimm.2011.04.003 (2011).
67. Haure-Mirande, J. V., Audrain, M., Ehrlich, M. E. & Gandy, S. Microglial

TYROBP/DAP12 in Alzheimer's disease: Transduction of physiological and pathological signals across TREM2. *Molecular Neurodegeneration* vol. 17 Preprint at https://doi.org/10.1186/s13024-022-00552-w (2022).

68. Pottier, C. *et al.* TYROBP genetic variants in early-onset Alzheimer's disease. *Neurobiol Aging* **48**, 222.e9-222.e15 (2016).
69. Neumann, H. & Daly, M. J. Variant TREM2 as Risk Factor for Alz hei mer's Disease. (2013) doi:10.1056/NEJMe1213157.
70. Stevens, B. *et al.* The Classical Complement Cascade Mediates CNS Synapse Elimination. *Cell* **131**, (2007).
71. Paolicelli, R. C. & Ferretti, M. T. Function and dysfunction of microglia during brain development: Consequences for synapses and neural circuits. *Frontiers in Synaptic Neuroscience* vol. 9 Preprint at https://doi.org/10.3389/fnsyn.2017.00009 (2017).
72. Audrain, M. *et al.* Integrative approach to sporadic Alzheimer's disease: deficiency of TYROBP in a tauopathy mouse model reduces C1q and normalizes clinical phenotype while increasing spread and state of phosphorylation of tau. *Mol Psychiatry* **24**, (2019).
73. Haure-Mirande, J. V. *et al.* Deficiency of TYROBP, an adapter protein for TREM2 and CR3 receptors, is neuroprotective in a mouse model of early Alzheimer's pathology. *Acta Neuropathol* **134**, 769–788 (2017).
74. Haure-Mirande, J. V. *et al.* Integrative approach to sporadic Alzheimer's disease: deficiency of TYROBP in cerebral Aβ amyloidosis mouse normalizes clinical phenotype and complement subnetwork molecular pathology without reducing Aβ burden. *Molecular Psychiatry 2018 24:3* **24**, 431–446 (2018).
75. Neniskyte, U. & Gross, C. T. Errant gardeners: glial-cell-dependent synaptic pruning and neurodevelopmental disorders. *Nature Reviews Neuroscience 2017 18:11* **18**, 658–670 (2017).
76. Hu, Y. *et al.* Wogonin mitigates microglia-mediated synaptic over-pruning and cognitive impairment following epilepsy. *Phytomedicine* **135**, 156222 (2024).
77. Wu, X. *et al.* Complement C1q drives microglia-dependent synaptic loss and cognitive impairments in a mouse model of lipopolysaccharide-induced neuroinflammation. *Neuropharmacology* **237**, (2023).
78. Bie, B., Wu, J., Foss, J. F. & Naguib, M. Activation of mGluR1 Mediates C1q-Dependent Microglial Phagocytosis of Glutamatergic Synapses in Alzheimer's Rodent Models. *Mol Neurobiol* **56**, 5568–5585 (2019).
79. Wu, J., Bie, B., Foss, J. F. & Naguib, M. Amyloid Fibril–Induced Astrocytic Glutamate Transporter Disruption Contributes to Complement C1q-Mediated Microglial Pruning of Glutamatergic Synapses. *Mol Neurobiol* **57**, 2290–2300 (2020).
80. Iweka, C. A. *et al.* Myeloid deficiency of the intrinsic clock protein BMAL1 accelerates cognitive aging by disrupting microglial synaptic pruning. *J Neuroinflammation* **20**, 1–16 (2023).

81. Andoh, M., Ikegaya, Y. & Koyama, R. Synaptic pruning by microglia in epilepsy. *Journal of Clinical Medicine* vol. 8 Preprint at https://doi.org/10.3390/jcm8122170 (2019).
82. Yuan, P. *et al.* PLD3 affects axonal spheroids and network defects in Alzheimer's disease. *Nature 2022 612:7939* **612**, 328–337 (2022).
83. Stefanescu, R. A., Shivakeshavan, R. G. & Talathi, S. S. Computational models of epilepsy. *Seizure* **21**, 748–759 (2012).
84. Fritschy, J. M. Epilepsy, E/I balance and GABAA receptor plasticity. *Front Mol Neurosci* **1**, 201 (2008).
85. Ren, X., Brodovskaya, A., Hudson, J. L. & Kapur, J. Connectivity and Neuronal Synchrony during Seizures. *Journal of Neuroscience* **41**, 7623–7635 (2021).
86. van Nifterick, A. M. *et al.* Functional network disruption in cognitively unimpaired autosomal dominant Alzheimer's disease: a magnetoencephalography study. *Brain Commun* **6**, (2024).
87. Luo, L. Architectures of neuronal circuits. *Science (1979)* **373**, (2021).
88. Dzyubenko, E. *et al.* Inhibitory control in neuronal networks relies on the extracellular matrix integrity. *Cellular and Molecular Life Sciences* **78**, 5647–5663 (2021).
89. Dejanovic, B. *et al.* Complement C1q-dependent excitatory and inhibitory synapse elimination by astrocytes and microglia in Alzheimer's disease mouse models. *Nat Aging* **2**, (2022).
90. Fan, J. *et al.* Preferential pruning of inhibitory synapses by microglia contributes to alteration of the balance between excitatory and inhibitory synapses in the hippocampus in temporal lobe epilepsy. *CNS Neurosci Ther* **29**, 2884–2900 (2023).
91. Holden, S. S. *et al.* Complement factor C1q mediates sleep spindle loss and epileptic spikes after mild brain injury. *Science (1979)* **373**, (2021).
92. Chu, Y. *et al.* Enhanced synaptic connectivity and epilepsy in C1q knockout mice. *Proc Natl Acad Sci U S A* **107**, (2010).
93. Ma, Y., Ramachandran, A., Ford, N., Parada, I. & Prince, D. A. Remodeling of dendrites and spines in the C1q knockout model of genetic epilepsy. *Epilepsia* **54**, (2013).
94. Chin, J. & Scharfman, H. E. Shared cognitive and behavioral impairments in epilepsy and Alzheimer's disease and potential underlying mechanisms. *Epilepsy & Behavior* **26**, 343–351 (2013).

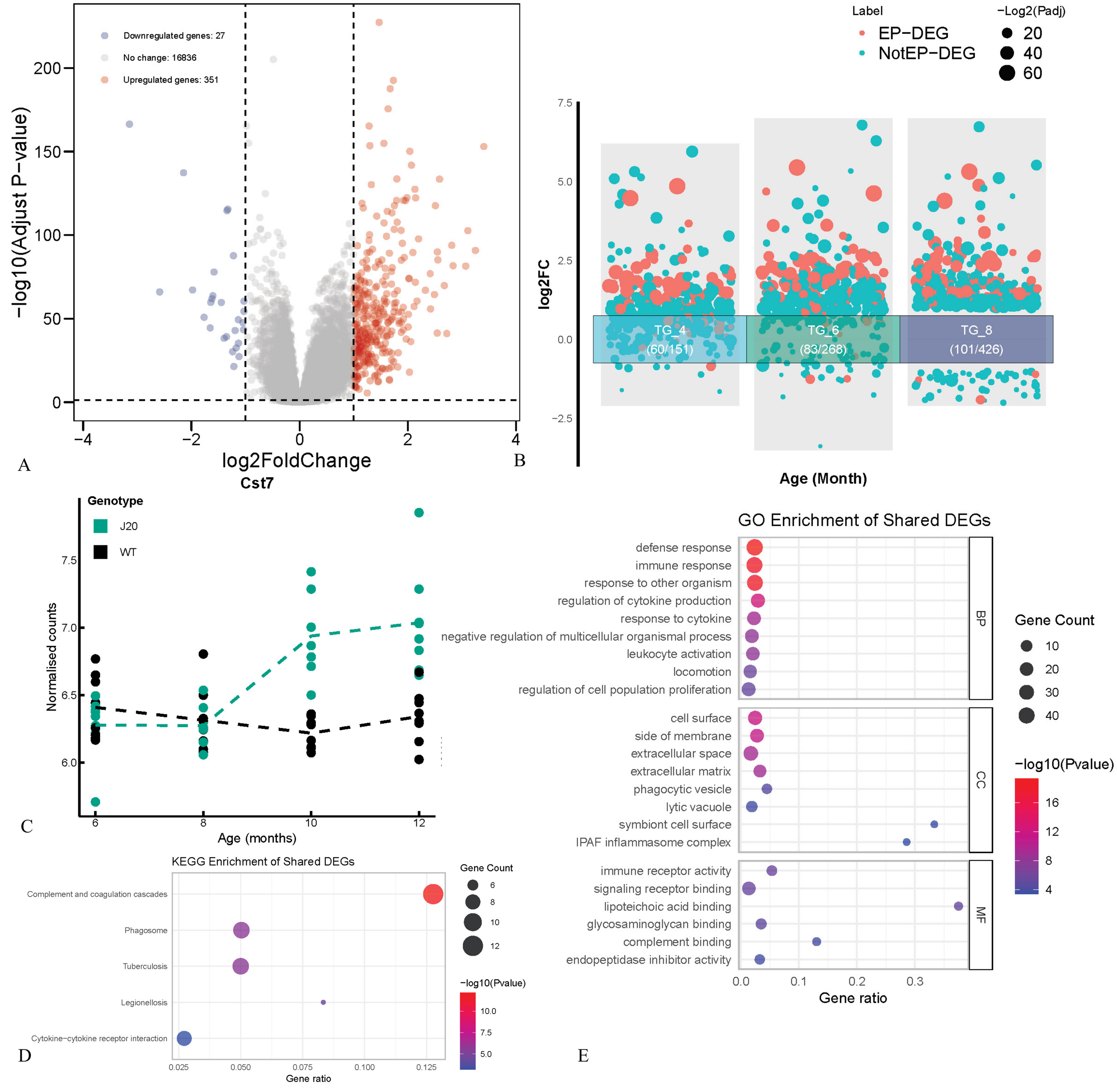
Downregulated genes: 27
No change: 16836
Upregulated genes: 351
−log10(Adjust P−value)
log2FoldChange
A
Label
EP−DEG
NotEP−DEG
−Log2(Padj)
20
40
60
log2FC
TG_4
(60/151)
TG_6
(83/268)
TG_8
(101/426)
Age (Month)
B
Genotype
J20
WT
Normalised counts
Age (months)
C
KEGG Enrichment of Shared DEGs
Complement and coagulation cascades
Phagosome
Tuberculosis
Legionellosis
Cytokine−cytokine receptor interaction
Gene ratio
Gene Count
−log10(Pvalue)
D
GO Enrichment of Shared DEGs
defense response
immune response
response to other organism
regulation of cytokine production
response to cytokine
negative regulation of multicellular organismal process
leukocyte activation
locomotion
regulation of cell population proliferation
BP
cell surface
side of membrane
extracellular space
extracellular matrix
phagocytic vesicle
lytic vacuole
symbiont cell surface
IPAF inflammasome complex
CC
immune receptor activity
signaling receptor binding
lipoteichoic acid binding
glycosaminoglycan binding
complement binding
endopeptidase inhibitor activity
MF
Gene ratio
Gene Count
−log10(Pvalue)
E

Figure 1

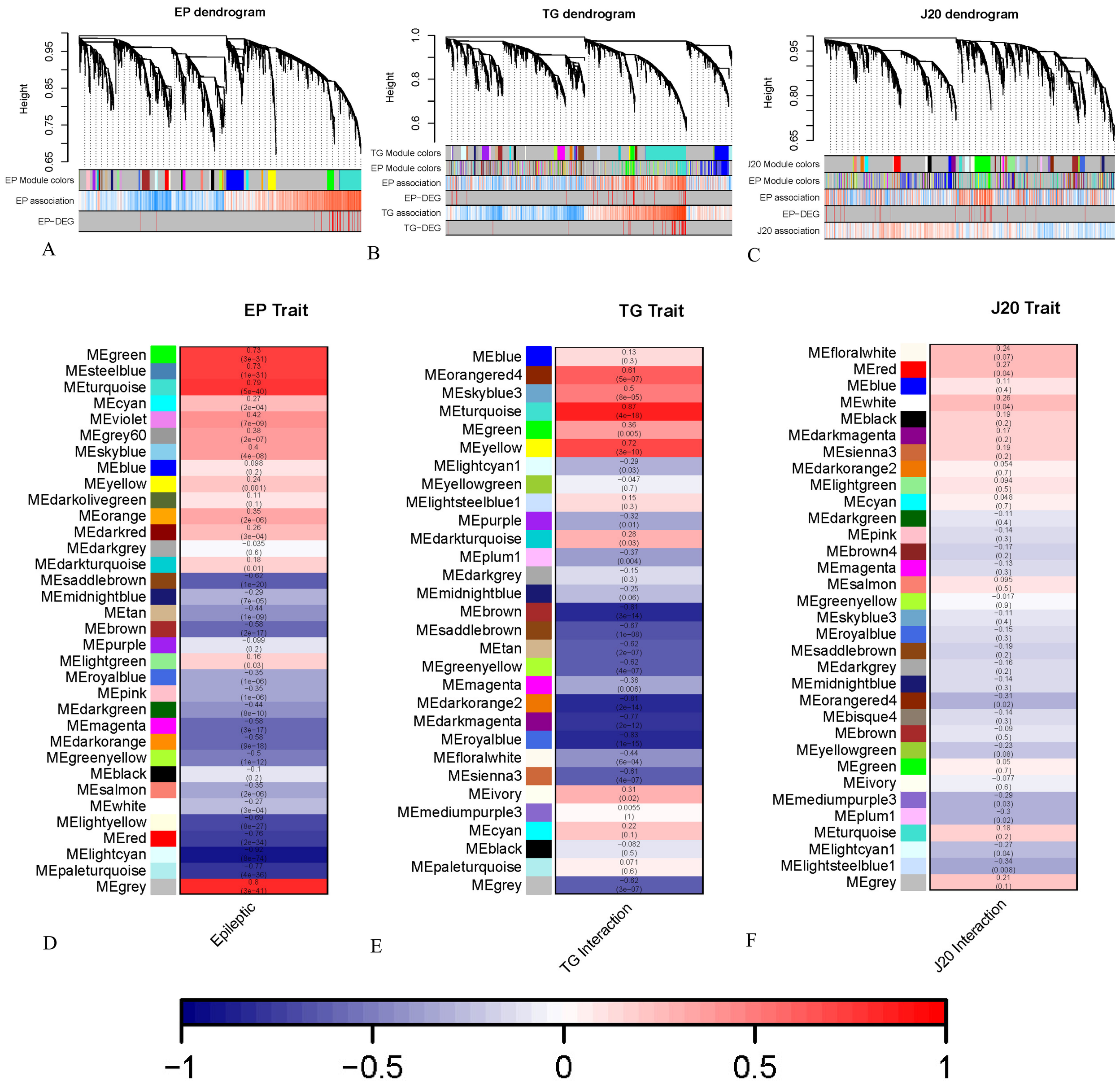
EP dendrogram
Height
0.65
0.75
0.85
0.95
EP Module colors
EP association
EP-DEG
A
TG dendrogram
Height
0.6
0.8
1.0
TG Module colors
EP Module colors
EP association
EP-DEG
TG association
TG-DEG
B
J20 dendrogram
Height
0.65
0.80
0.95
J20 Module colors
EP Module colors
EP association
EP-DEG
J20 association
C
EP Trait
MEgreen 0.73 (3e-31)
MEsteelblue 0.73 (1e-31)
MEturquoise 0.79 (5e-40)
MEcyan 0.27 (2e-04)
MEviolet 0.42 (7e-09)
MEgrey60 0.38 (2e-07)
MEskyblue 0.4 (4e-08)
MEblue 0.098 (0.2)
MEyellow 0.24 (0.001)
MEdarkolivegreen 0.11 (0.1)
MEorange 0.35 (2e-06)
MEdarkred 0.26 (3e-04)
MEdarkgrey -0.035 (0.6)
MEdarkturquoise 0.18 (0.01)
MEsaddlebrown -0.62 (1e-20)
MEmidnightblue -0.29 (7e-05)
MEtan -0.44 (1e-09)
MEbrown -0.58 (2e-17)
MEpurple -0.099 (0.2)
MElightgreen 0.16 (0.03)
MEroyalblue -0.35 (1e-06)
MEpink -0.35 (1e-06)
MEdarkgreen -0.44 (8e-10)
MEmagenta -0.58 (3e-17)
MEdarkorange -0.58 (9e-18)
MEgreenyellow -0.5 (1e-12)
MEblack -0.1 (0.2)
MEsalmon -0.35 (2e-06)
MEwhite -0.27 (3e-04)
MElightyellow -0.69 (8e-27)
MEred -0.76 (2e-34)
MElightcyan -0.92 (8e-74)
MEpaleturquoise -0.77 (4e-36)
MEgrey 0.8 (3e-41)
Epileptic
D
TG Trait
MEblue 0.13 (0.3)
MEorangered4 0.61 (5e-07)
MEskyblue3 0.5 (8e-05)
MEturquoise 0.87 (4e-18)
MEgreen 0.36 (0.005)
MEyellow 0.72 (3e-10)
MElightcyan1 -0.29 (0.03)
MEyellowgreen -0.047 (0.7)
MElightsteelblue1 0.15 (0.3)
MEpurple -0.32 (0.01)
MEdarkturquoise 0.28 (0.03)
MEplum1 -0.37 (0.004)
MEdarkgrey -0.15 (0.3)
MEmidnightblue -0.25 (0.06)
MEbrown -0.81 (3e-14)
MEsaddlebrown -0.67 (1e-08)
MEtan -0.62 (2e-07)
MEgreenyellow -0.62 (4e-07)
MEmagenta -0.36 (0.006)
MEdarkorange2 -0.81 (2e-14)
MEdarkmagenta -0.77 (2e-12)
MEroyalblue -0.83 (1e-15)
MEfloralwhite -0.44 (6e-04)
MEsienna3 -0.61 (4e-07)
MEivory 0.31 (0.02)
MEmediumpurple3 0.0055 (1)
MEcyan 0.22 (0.1)
MEblack -0.082 (0.5)
MEpaleturquoise 0.071 (0.6)
MEgrey -0.62 (3e-07)
TG Interaction
E
J20 Trait
MEfloralwhite 0.24 (0.07)
MEred 0.27 (0.04)
MEblue 0.11 (0.4)
MEwhite 0.26 (0.04)
MEblack 0.19 (0.2)
MEdarkmagenta 0.17 (0.2)
MEsienna3 0.19 (0.2)
MEdarkorange2 0.054 (0.7)
MElightgreen 0.094 (0.5)
MEcyan 0.048 (0.7)
MEdarkgreen -0.11 (0.4)
MEpink -0.14 (0.3)
MEbrown4 -0.17 (0.2)
MEmagenta -0.13 (0.3)
MEsalmon 0.095 (0.5)
MEgreenyellow -0.017 (0.9)
MEskyblue3 -0.11 (0.4)
MEroyalblue -0.15 (0.3)
MEsaddlebrown -0.19 (0.2)
MEdarkgrey -0.16 (0.2)
MEmidnightblue -0.14 (0.3)
MEorangered4 -0.31 (0.02)
MEbisque4 -0.14 (0.3)
MEbrown -0.09 (0.5)
MEyellowgreen -0.23 (0.08)
MEgreen 0.05 (0.7)
MEivory -0.077 (0.6)
MEmediumpurple3 -0.29 (0.03)
MEplum1 -0.3 (0.02)
MEturquoise 0.18 (0.2)
MElightcyan1 -0.27 (0.04)
MElightsteelblue1 -0.34 (0.008)
MEgrey 0.21 (0.1)
J20 Interaction
F
-1
-0.5
0
0.5
1

Figure 2

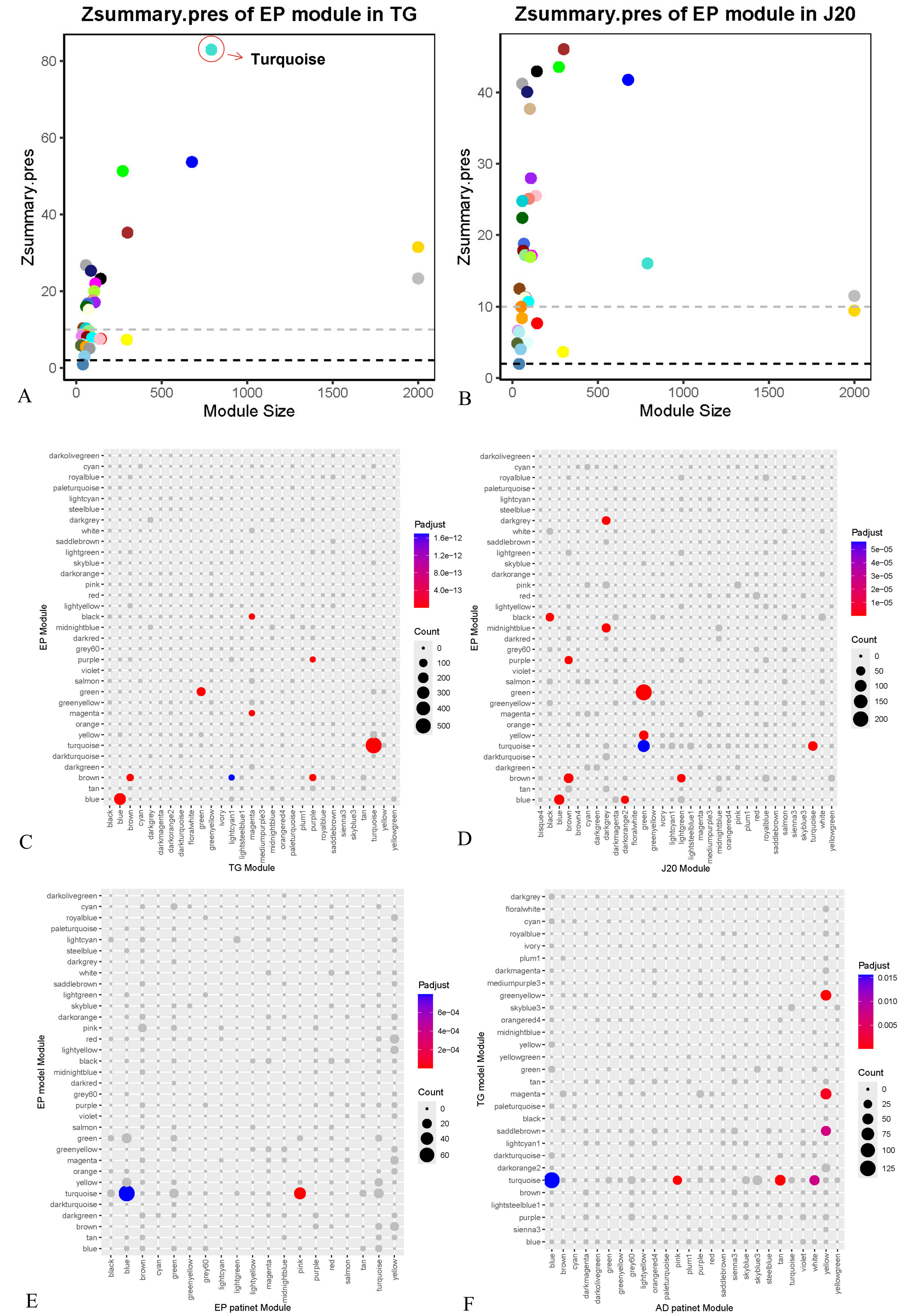
Zsummary.pres of EP module in TG
Turquoise
Zsummary.pres
Module Size
A
Zsummary.pres of EP module in J20
Zsummary.pres
Module Size
B
EP Module
TG Module
Padjust
Count
C
EP Module
J20 Module
Padjust
Count
D
EP model Module
EP patinet Module
Padjust
Count
E
TG model Module
AD patinet Module
Padjust
Count
F

Figure 3

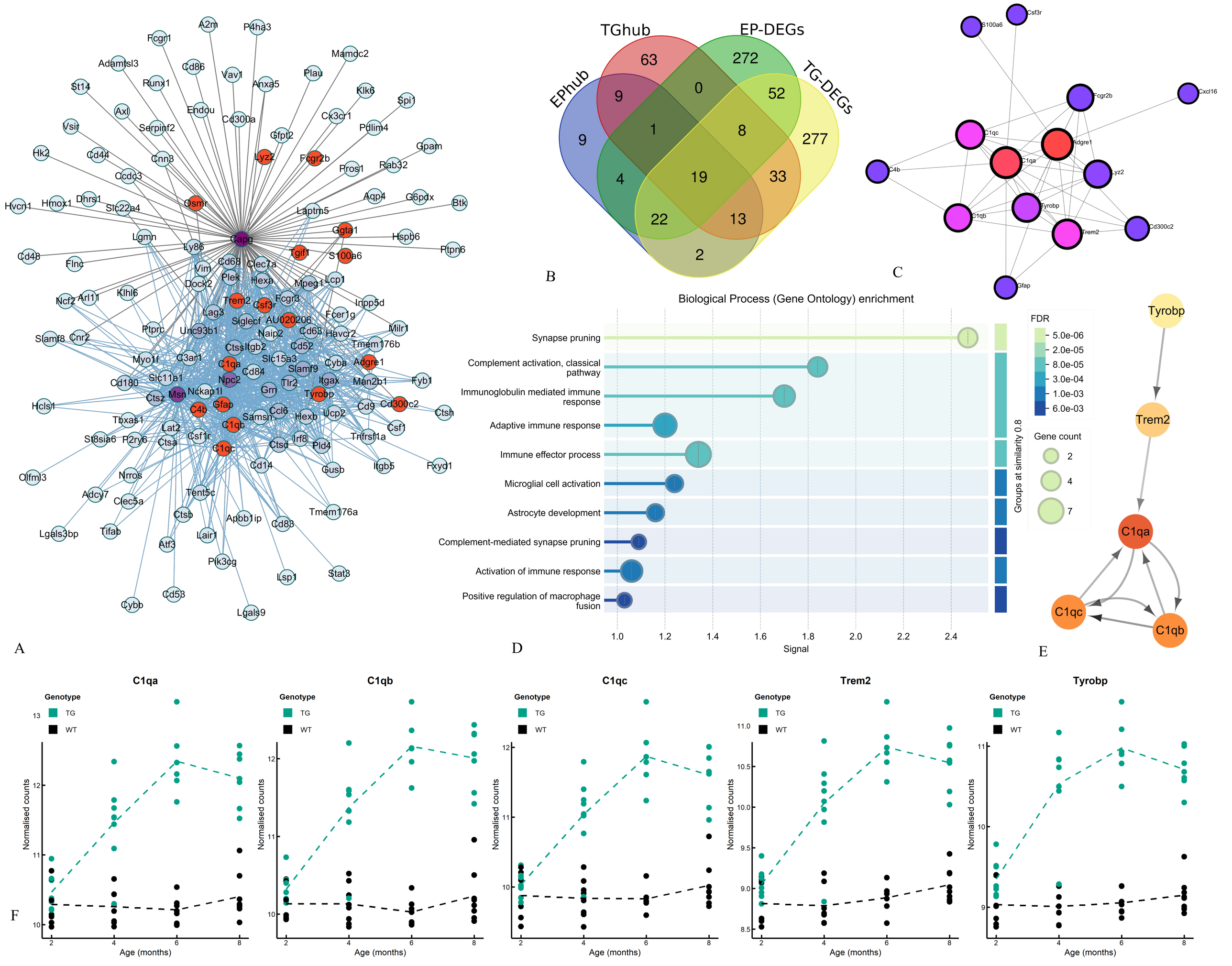
A
B
C
D
E
F
TGhub
EP-DEGs
EPhub
TG-DEGs
63
272
9
0
52
9
1
8
277
4
19
33
22
13
2
Biological Process (Gene Ontology) enrichment
Synapse pruning
Complement activation, classical pathway
Immunoglobulin mediated immune response
Adaptive immune response
Immune effector process
Microglial cell activation
Astrocyte development
Complement-mediated synapse pruning
Activation of immune response
Positive regulation of macrophage fusion
Signal
Groups at similarity 0.8
FDR
5.0e-06
2.0e-05
8.0e-05
3.0e-04
1.0e-03
6.0e-03
Gene count
2
4
7
Tyrobp
Trem2
C1qa
C1qc
C1qb
C1qa
C1qb
C1qc
Trem2
Tyrobp
Genotype
TG
WT
Normalised counts
Age (months)

Figure 4

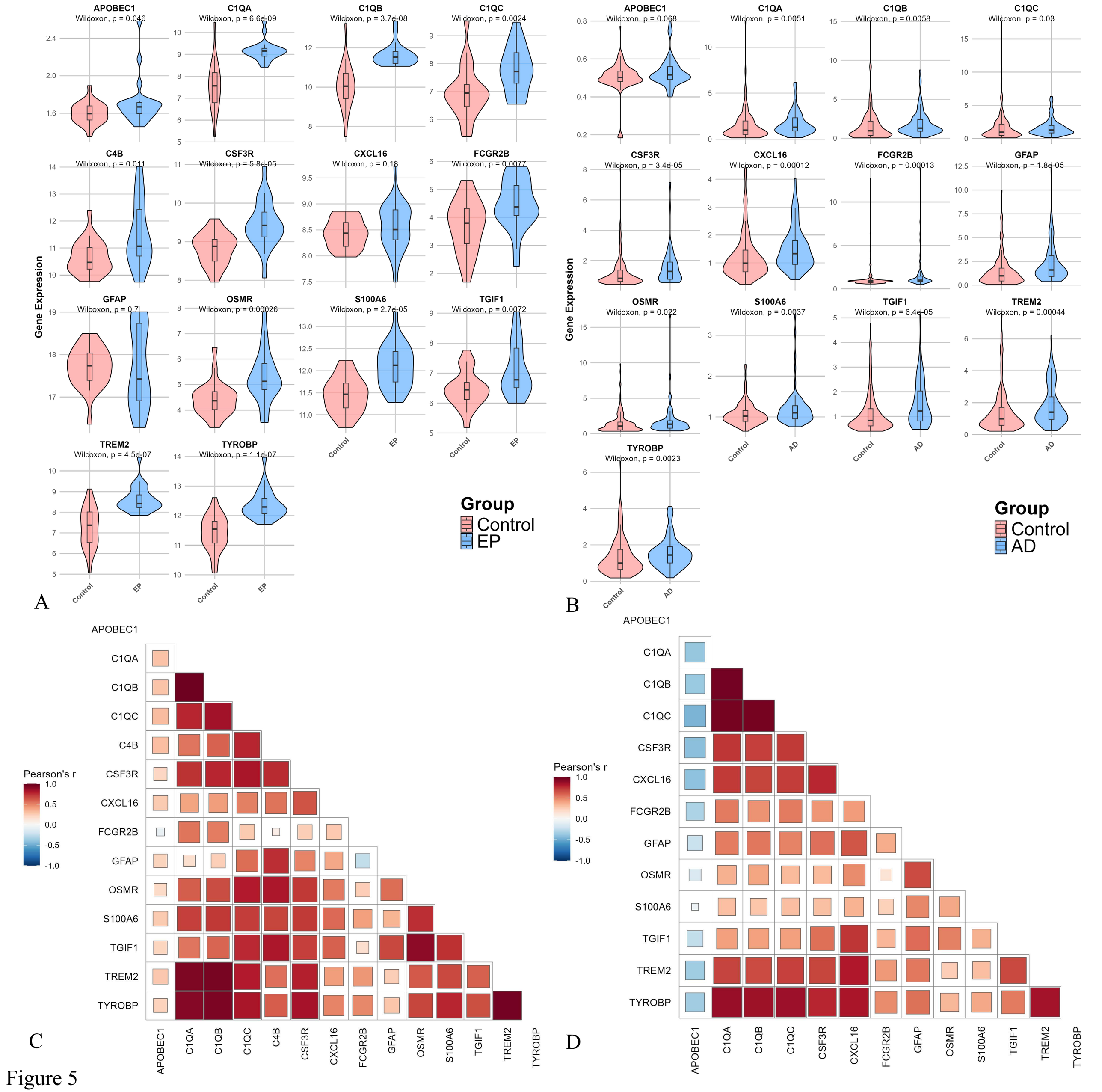
A
Gene Expression
APOBEC1 Wilcoxon, p = 0.046
C1QA Wilcoxon, p = 6.6e-09
C1QB Wilcoxon, p = 3.7e-08
C1QC Wilcoxon, p = 0.0024
C4B Wilcoxon, p = 0.011
CSF3R Wilcoxon, p = 5.8e-05
CXCL16 Wilcoxon, p = 0.18
FCGR2B Wilcoxon, p = 0.0077
GFAP Wilcoxon, p = 0.7
OSMR Wilcoxon, p = 0.00026
S100A6 Wilcoxon, p = 2.7e-05
TGIF1 Wilcoxon, p = 0.0072
TREM2 Wilcoxon, p = 4.5e-07
TYROBP Wilcoxon, p = 1.1e-07
Control
EP
Group
Control
EP
B
Gene Expression
APOBEC1 Wilcoxon, p = 0.068
C1QA Wilcoxon, p = 0.0051
C1QB Wilcoxon, p = 0.0058
C1QC Wilcoxon, p = 0.03
CSF3R Wilcoxon, p = 3.4e-05
CXCL16 Wilcoxon, p = 0.00012
FCGR2B Wilcoxon, p = 0.00013
GFAP Wilcoxon, p = 1.8e-05
OSMR Wilcoxon, p = 0.022
S100A6 Wilcoxon, p = 0.0037
TGIF1 Wilcoxon, p = 6.4e-05
TREM2 Wilcoxon, p = 0.00044
TYROBP Wilcoxon, p = 0.0023
Control
AD
Group
Control
AD
C
Pearson's r
1.0
0.5
0.0
-0.5
-1.0
APOBEC1
C1QA
C1QB
C1QC
C4B
CSF3R
CXCL16
FCGR2B
GFAP
OSMR
S100A6
TGIF1
TREM2
TYROBP
D
Pearson's r
1.0
0.5
0.0
-0.5
-1.0
APOBEC1
C1QA
C1QB
C1QC
CSF3R
CXCL16
FCGR2B
GFAP
OSMR
S100A6
TGIF1
TREM2
TYROBP

Figure 5

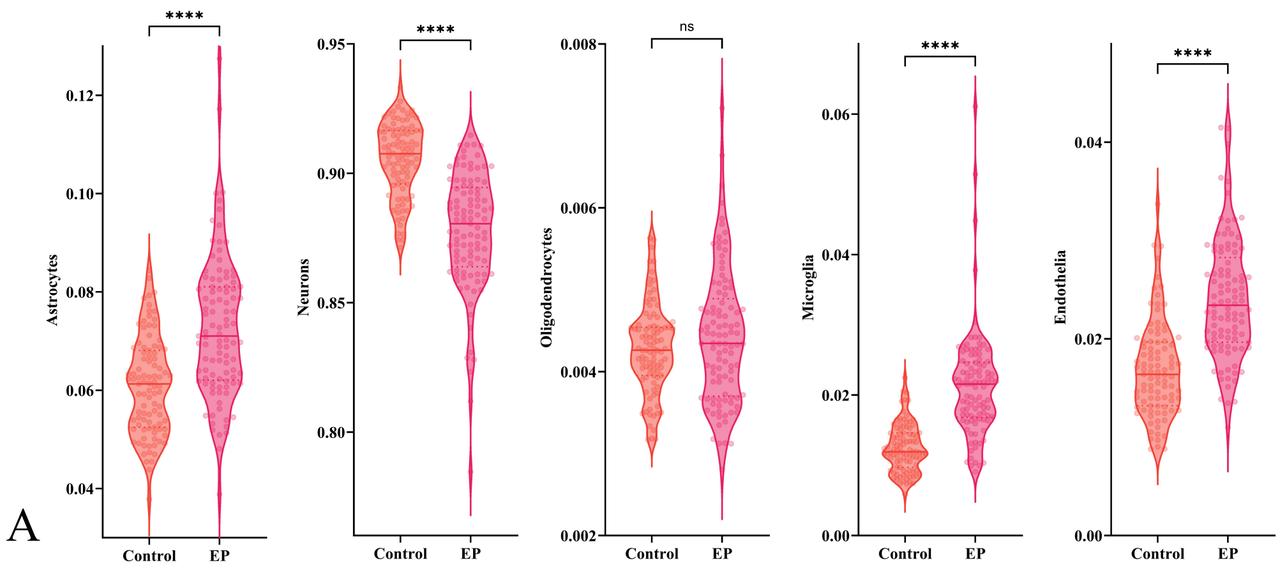
A
Astrocytes
Neurons
Oligodendrocytes
Microglia
Endothelia
Control
EP
****
ns

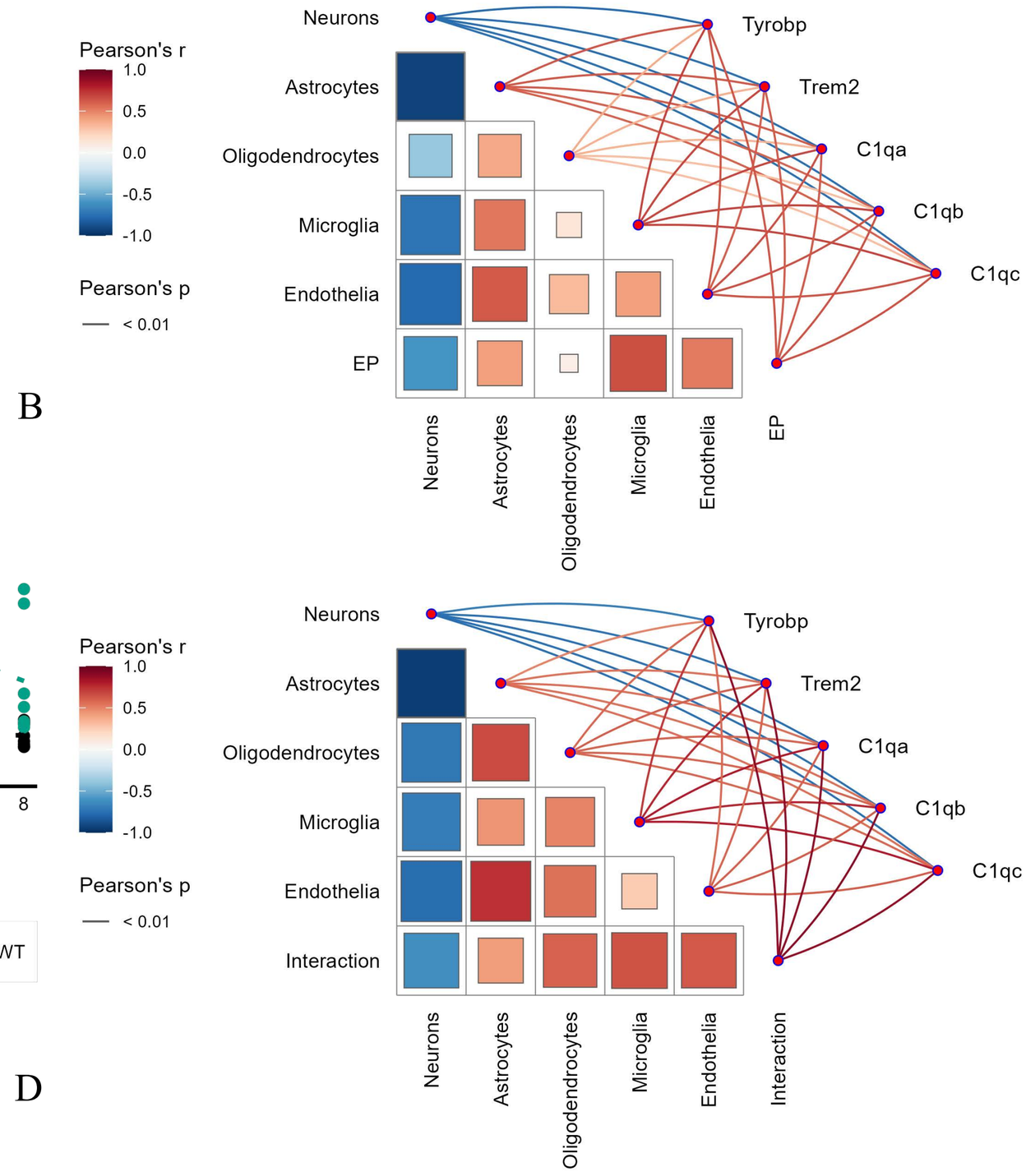
B
Pearson's r
1.0
0.5
0.0
-0.5
-1.0
Pearson's p
< 0.01
Neurons
Astrocytes
Oligodendrocytes
Microglia
Endothelia
EP
Tyrobp
Trem2
C1qa
C1qb
C1qc
D
Interaction

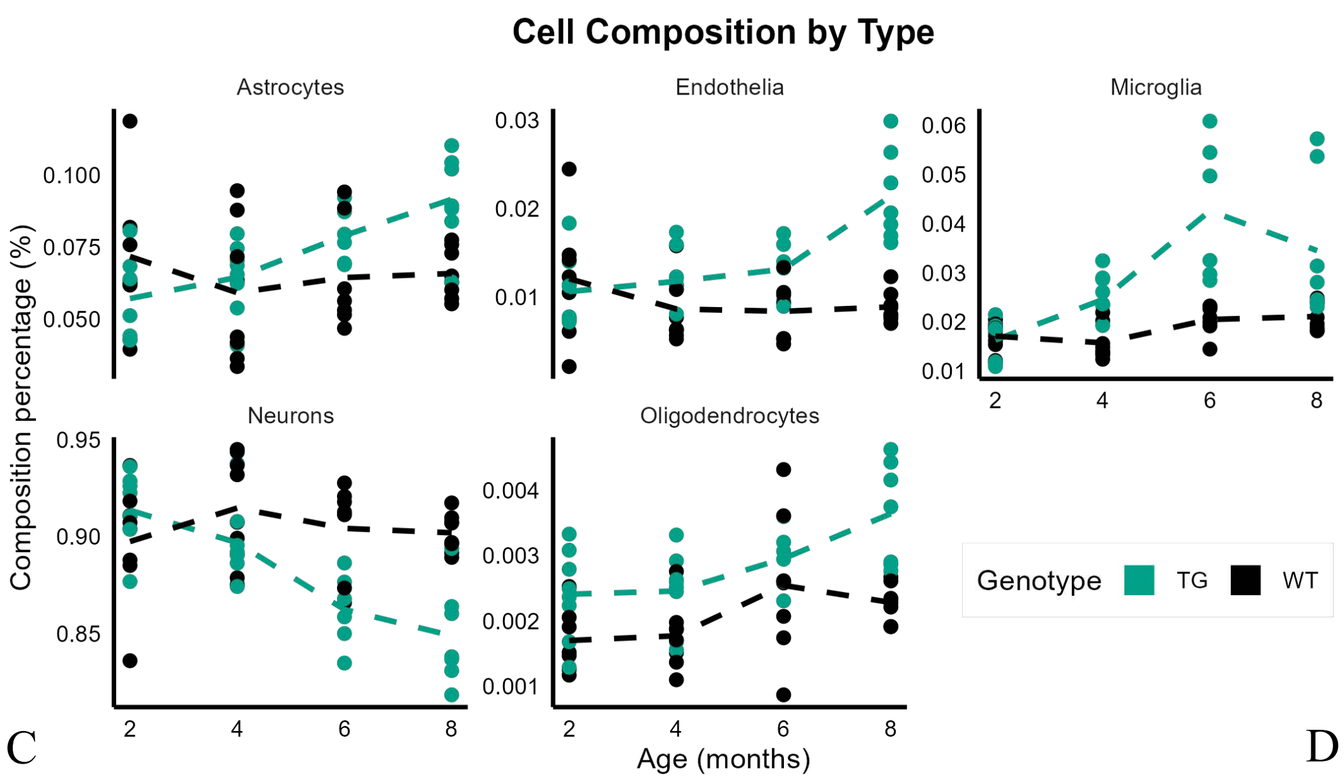
Cell Composition by Type
C
Astrocytes
Endothelia
Microglia
Neurons
Oligodendrocytes
Composition percentage (%)
Age (months)
Genotype
TG
WT

Figure 6

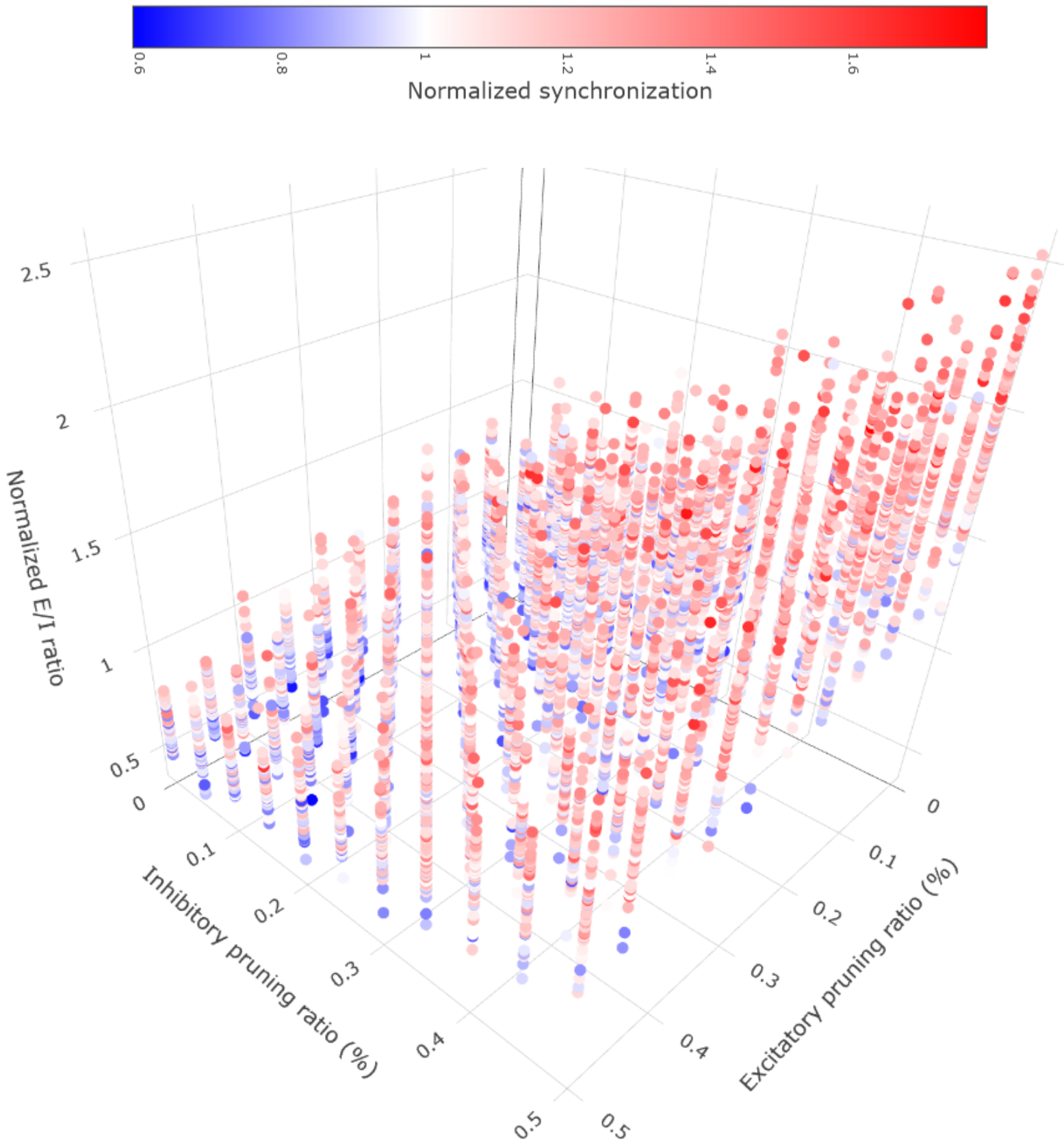
0.6
0.8
1
1.2
1.4
1.6
Normalized synchronization
Normalized E/I ratio
2.5
2
1.5
1
0.5
0
Inhibitory pruning ratio (%)
0.1
0.2
0.3
0.4
0.5
Excitatory pruning ratio (%)
0
0.1
0.2
0.3
0.4
0.5

Figure 7